Role of Oil Palm Empty Fruit Bunch-Derived Cellulose in Improving the Sonocatalytic Activity of Silver-Doped Titanium Dioxide

Yi Ding Chai [1], Yean Ling Pang [1,2,*], Steven Lim [1,2], Woon Chan Chong [1,2], Chin Wei Lai [3] and Ahmad Zuhairi Abdullah [4]

[1] Department of Chemical Engineering, Lee Kong Chian Faculty of Engineering and Science, Universiti Tunku Abdul Rahman, Kajang 43000, Malaysia; nicoleyd@1utar.my (Y.D.C.); stevenlim@utar.edu.my (S.L.); chongwchan@utar.edu.my (W.C.C.)

[2] Centre for Photonics and Advanced Materials Research, Universiti Tunku Abdul Rahman, Kajang 43000, Malaysia

[3] Nanotechnology and Catalysis Research Centre (NANOCAT), Institute of Advanced Studies (IAS), Universiti Malaya, Kuala Lumpur 50603, Malaysia; cwlai@um.edu.my

[4] School of Chemical Engineering, Universiti Sains Malaysia, Nibong Tebal 14300, Malaysia; chzuhairi@usm.my

* Correspondence: pangyl@utar.edu.my or pangyeanling@hotmail.com; Tel.: +60-39086-0288; Fax: +60-39019-8868

Abstract: In this study, a novel cellulose/Ag/TiO$_2$ nanocomposite was successfully synthesized via the hydrothermal method. The cellulose extracted from oil palm empty fruit bunch (OPEFB) could address the disposal issue created by OPEFB biomass. Characterization studies such as FESEM, EDX, HRTEM, XRD, FTIR, UV–Vis DRS, PL, XPS, and surface analysis were conducted. It was observed that the incorporation of cellulose could hinder the agglomeration, reduce the band gap energy to 3 eV, increase the specific surface area to 150.22 m^3/g, and lower the recombination rate of the generated electron-hole pairs compared to Ag/TiO$_2$ nanoparticles. The excellent properties enhance the sonocatalytic degradation efficiency of 10 mg/L Congo red (up to 81.3% after 10 min ultrasonic irradiation) in the presence of 0.5 g/L cellulose/Ag/TiO$_2$ at 24 kHz and 280 W. The improvement of catalytic activity was due to the surface plasmon resonance effect of Ag and numerous hydroxyl groups on cellulose that capture the holes, which delay the recombination rate of the charge carriers in TiO$_2$. This study demonstrated an alternative approach in the development of an efficient sonocatalyst for the sonocatalytic degradation of Congo red.

Keywords: titanium dioxide; cellulose; silver doping; sonocatalysis; Congo red

1. Introduction

The textile industry is the main contributor to dye pollution. The annual effluent of textile industry was estimated at approximately 100,000 tons of dyes [1]. There are more than 10,000 types of dye that are commercially available and azo dyes are the most used dye in the industry (60–70%) [2]. This is due to their simple and versatile synthesis, high dyeing ability, and chemical stability. In general, azo dyes comprise at least one azo group bonded with aromatic rings that contain functional groups such as amino, methyl, and sulfonic acids [3]. The π conjugated bonds and resonance in the aromatic structure contributed to its high stability [2]. Azo dyes are hazardous contaminants that produce mutagenic and carcinogenic compounds such as aromatic amines when released into the environment [4]. Therefore, conventional treatments are insufficient for degrading them because they are resistant to acid/alkali and light irradiation.

Advanced oxidation processes (AOPs) such as sonolysis, ozonation, and Fenton oxidation are known to generate various types of reactive oxygen species that can rapidly oxidize the contaminants. Ultrasonic irradiation has received considerable attention due

to its high penetrability in liquid medium, environmental friendliness, low cost, and zero sludge formation [3,5]. Acoustic cavitation is the key factor in ultrasonic irradiation due to the generation, growth, and explosive collapse of bubbles [6]. During the collapsing of bubbles, the generated shock waves from the nanosecond implosions will increase local temperature (5000 K) and pressure (1000 atm) [5]. Water molecules are then thermally dissociated into hydroxyl ($\bullet$OH) and hydrogen (H^+) radicals. Eventually, these highly reactive radicals will attack the organic pollutants and transform them into water, carbon dioxide, and inorganic salts.

Among these semiconductors, titanium dioxide (TiO_2) is widely used as a heterogeneous catalyst owing to its chemical properties such as low toxicity, low cost, and high chemical stability [7]. Nevertheless, TiO_2 could not be excited by the visible light due to its wide band gap energy (3.2 eV). The rapid recombination rate of electron-hole pairs (within nanosecond) can influence its catalytic efficiency [8]. To overcome these shortcomings, TiO_2 can be modified with metal/non-metal doping [9–11], semiconductor coupling [12], and semiconductor photosensitization [13]. Among these approaches, silver (Ag) doping was chosen in this study as Ag can serve as a prominent plasmonic material for sensitizing TiO_2. Moreover, Ag is generally cheap and exhibits low toxicity and high antibacterial ability than compared to gold and platinum [14]. The incorporation of an appropriate amount of Ag can reduce the band gap energy of TiO_2 and inhibit the recombination of electron-hole pairs by trapping the electrons due to the prominent surface plasmon resonance [15].

Recently, the conversions and utilization of agricultural biomass into higher value-added products to minimize the massive quantity of waste and to fulfill the concept of circular economy are attracting attention [16]. Agricultural biomass consists mostly of cellulose, hemicellulose and lignin. Cellulose is attractive due to its abundancy, renewability, zero toxicity, remarkable mechanical strength, biodegradability, and biocompatibility [17]. It contains several types of functional groups such as hydroxyl (–OH) and carboxyl groups. Pollutants can be adsorbed through the electrostatic interaction of the contaminant structure with these oxygen-containing functional groups. Furthermore, the addition of cellulose with high functional groups on semiconductors can increase surface area and enable well dispersion of Ag/TiO_2 nanoparticles by reducing agglomeration. Subsequently, this introduces additional active sites and eventually enhances catalytic activity [18]. The synergistic effect of the cellulose-TiO_2 composites has attracted the interest of researchers to develop new catalysts for the remediation of wastewater.

The present work demonstrated the investigation of oil palm empty fruit bunch (OPEFB) biomass-based cellulose/Ag/TiO_2 composites for the enhancement of sonocatalytic degradation of Congo red for the first-time. This novel catalyst was able to address the problems faced by using the bare TiO_2 such as wide band gap energy, rapid recombination rate of electron-hole pairs in pure TiO_2, and agglomeration phenomenon experienced by the Ag/TiO_2 nanoparticles. Moreover, it was reported that OPEFB is a major biomass waste in palm oil mills, reaching about 20–23% of fresh fruit bunch [19]. This had created a critical disposal issue to the environment, and the huge amount of cellulose (30–50% by weight) contained in OPEFB can serve as a potential additive material in Ag/TiO_2 nanoparticles. The physicochemical properties of the synthesized samples were also characterized comprehensively through various types of characterization techniques such as field emission scanning electron microscopy (FESEM), energy dispersive X-Ray (EDX) analysis, high-resolution transmission electron microscopy (HRTEM), X-Ray diffraction analysis (XRD), Fourier transform infrared spectroscopy (FTIR), UV–vis diffuse reflectance spectroscopy (DRS), photoluminescence analysis (PL), X-ray photoelectron spectroscopy (XPS), and surface analysis. This was followed by catalytic performance analysis using the adsorption and sonocatalytic degradation of Congo red.

2. Materials and Methods

2.1. Materials

Sodium hydroxide (99%), n-hexane (96%), hydrochloric acid (37%), and silver sulfate ($\geq$98.5%) were purchased from Merck (Merck KGaA, Darmstadt, Germany). Next, sodium hypochlorite (2.4%) was purchased from Clorox (Oakland, CA, USA). Titanium (IV) isopropoxide (97%) was obtained from Sigma-Aldrich (St. Louis, MO, USA). Moreover, ethanol (95%) and Congo red (40%) were bought from R&M Chemicals (Selangor, Malaysia). All received chemicals were applied without extra purification. OPEFBs were collected from a palm mill located at Selangor, Malaysia. Lastly, distilled water was utilized throughout this research study.

2.2. Preparation of Cellulose

OPEFB was first cut into small fragments, washed thoroughly with distilled water, and immersed in n-hexane solution for 4 h in order to remove excess palm oil. These samples were oven dried at 70 °C for 24 h and ground into OPEFB fibers (<600 μm). The OPEFB fibers were then treated with ethanol for 60 min, rinsed with distilled water, and oven-dried at 100 °C overnight to eliminate wax and other impurities. The method for cellulose extraction from OPEFB fibers was modified based on a research study conducted by Lefatshe et al. [20]. The amount of 10 g of OPEFB fibers prepared earlier was treated with 4% w/w sodium hydroxide solution at 90 °C for 2 h in an alkali treatment in order to eliminate lignin and hemicellulose. These samples were treated with 10% *w/w* hydrochloric acid solution at 45 °C for 2 h to undergo acid hydrolysis in order to further remove the remaining hemicellulose content. Then, the samples were bleached with 2.4 wt% sodium hypochlorite solution at room temperature for 3 h in order to enhance physical outlook and to eliminate the residual lignin and hemicellulose. Lastly, the extracted cellulose was rinsed and oven dried at 100 °C for 24 h to remove excess moisture content.

2.3. Preparation of TiO$_2$, Cellulose/TiO$_2$, Ag/TiO$_2$, and Cellulose/Ag/TiO$_2$

The hydrothermal synthesis conditions for TiO$_2$, cellulose/TiO$_2$, Ag/TiO$_2$, and cellulose/Ag/TiO$_2$ were modified according to the research study conducted by Zhang et al. [21]. Initially, 9 mL of titanium (IV) isopropoxide was added into 41 mL of ethanol under stirring conditions for 30 min. The resultant solution was added dropwise into a 50% *w/w* ethanol solution under stirring conditions for 60 min. Silver sulfate was added into 50% *w/w* ethanol solution according to the mass ratio of Ag: TiO$_2$ equal to 0.05:1 under stirring conditions for 2 h. The Ag mixture was then added into the prepared TiO$_2$ solution under stirring condition for another 30 min. Ethanol acted as a cosolvent and a reducing agent to reduce Ag$^+$ to metallic Ag [22]. The amount of 0.1 M sodium hydroxide solution was added into the mixture under stirring conditions for 1 h in order to promote the reduction process [23]. The cellulose-ethanol suspension was prepared based on the mass ratio of cellulose: TiO$_2$ equal to 0.05:1. Next, the Ag-doped TiO$_2$ solution was added dropwise into the cellulose-ethanol solution under stirring conditions for 30 min. The final mixture was sonicated in a water bath for 30 min to minimize particle aggregation. The mixture was added into a Teflon-lined autoclave before hydrothermal synthesis. Lastly, the mixture was heated in the oven at 130 °C for 20 h. The solution was centrifuged to collect the final sample after cooling to room temperature. The final sample was oven-dried at 100 °C overnight and labelled as cellulose/Ag/TiO$_2$. The same procedure was conducted to prepare cellulose/TiO$_2$ at different mass ratios of 0.05:1, 0.25:1, 0.5:1, 0.9:1, and Ag/TiO$_2$ at different mass ratios of 0.01:1, 0.03:1, 0.1:1, and 0.15:1. Pure TiO$_2$ was also synthesized hydrothermally as control for comparison with other synthesized samples.

2.4. Sample Characterization

The surface morphology and elemental composition of the prepared samples (TiO$_2$, cellulose, 0.05 cellulose/TiO$_2$, 0.05 Ag/TiO$_2$, and cellulose/Ag/TiO$_2$) were studied by using FESEM (JEOL Ltd., Tokyo, Japan) and EDX (Hitachi Ltd., Tokyo, Japan), respectively.

Moreover, the high-resolution images of cellulose/Ag/TiO$_2$ were obtained by employing a Philips Model Tecnai 20 transmission electron microscope (Koninklijke Philips N.V., Amsterdam, Netherlands). The crystalline phase of the prepared samples was determined by using LabX XRD-6000 X-ray diffractometer (Shimadzu Corp., Tokyo, Japan) with CuKα radiation. The crystallite size was estimated by using the Debye–Scherrer equation based on the most intense peak found in the sample. A Thermo Scientific Nicolet iS10 Fourier transform infrared spectroscope (Thermo Fisher Scientific Inc., Waltham, MA, USA) was used to determine the functional groups on the catalyst. Moreover, surface analysis was conducted by utilizing a Micromeritics 3Flex surface characterization analyser (Micromeritics Instrument Corp., Norcross, GA, USA). The specific surface area of the samples was determined using the Brunauer–Emmett–Teller (BET) method based on nitrogen adsorption–desorption data at 77.35 K. Meanwhile, the pore size and pore volume were obtained based on the desorption of nitrogen isotherm using the Barrett–Joyner–Halenda (BJH) method. UV–Vis DRS was performed on the prepared samples to obtain the band gap energies by using a Perkin Elmer Lambda 35 UV–Vis spectrophotometer (PerkinElmer Inc., Waltham, MA, USA). In addition, the separation efficiencies of the generated electron-hole pairs were evaluated by using an Edinburgh FLS 920 Time Resolved Fluorescence Spectrometer (Edinburgh Instruments Ltd., Livingston, SCT, UK) with an excitation wavelength at 300 nm. An Omicron DAR 400 X-ray photoelectron spectroscope (Scienta Omicron Inc., Uppsala, Sweden) was used to investigate the surface chemical compositions and chemical and bonding states of the cellulose/Ag/TiO$_2$ with monochromatized Al Kα at a binding energy of 1486.7 eV as the X-ray source.

2.5. Adsorption and Sonocatalytic Degradation of Congo Red

The sonocatalytic activities of the prepared samples (cellulose/TiO$_2$ and Ag/TiO$_2$ at different mass ratio, followed by TiO$_2$, cellulose, 0.05 cellulose/TiO$_2$, 0.05 Ag/TiO$_2$, and cellulose/Ag/TiO$_2$) were evaluated by using the removal of Congo red under ultrasound irradiation. In a typical experiment, 0.5 g/L of catalyst was added into 10 mg/L of Congo red solution to study the catalytic performance. The dye solution containing catalysts was left in the dark for 30 min of pre-adsorption to reach adsorption–desorption equilibrium. The ultrasonic irradiation with ultrasonic frequency of 24 kHz and power of 280 W was introduced to the dye solution by using a Hielscher Model UP400S ultrasonic processor. The ultrasonic probe was inserted into the dye solution to perform the sonocatalytic degradation of dye. The collected dye samples were centrifuged at 10,000 rpm for 10 min to separate the catalyst. A Jenway Model 6320D UV–Vis spectrophotometer was used to determine the residual concentration of Congo red samples at a maximum absorbance of 497 nm. The degradation efficiency of Congo red was calculated based on Equation (1):

$$\text{Degradation efficiency (\%)} = (C_0 - C_t)/C_0 \times 100\% \qquad (1)$$

where C_0 is the initial dye concentration (mg/L) before sonocatalysis process, and C_t is the resultant dye concentration at time t. All experiments were repeated 3 times to determine the error bar for the sample data. Chemical oxygen demand (COD) test was conducted to observe the COD removal in Congo red upon 60 min of ultrasonic irradiation. No catalyst reusability and stability tests were conducted in this study as the scope was only focused on the as-prepared catalysts' characterization and sonocatalytic performance rather than regeneration studies.

3. Results and Discussion

3.1. Characterization Study

3.1.1. FESEM, HRTEM and EDX

Figure 1 shows the surface morphology of cellulose, TiO$_2$, 0.05 cellulose/TiO$_2$, 0.05 Ag/TiO$_2$, and cellulose/Ag/TiO$_2$. It was observed that the TiO$_2$ nanomaterials were spherical shapes with an average size ranging from 10 to 15 nm as shown in Figure 1a. These nanoparticles were agglomerated to a size range of 200–500 nm. The formation

of nanoparticles cluster was due to the reduction in surface energy to improve their stability [24]. Meanwhile, cellulose presented a smooth surface with no cracks observed, as shown in Figure 1b, which might be attributed to the hydrogen bond linkage. This result also demonstrated that the acid extraction of cellulose was unable to develop sufficient porosity on the cellulose structure. A similar finding was obtained by Zhang et al. [25], where the smooth surface of isolated cellulose from pine wood biomass was observed between the fibril bundles.

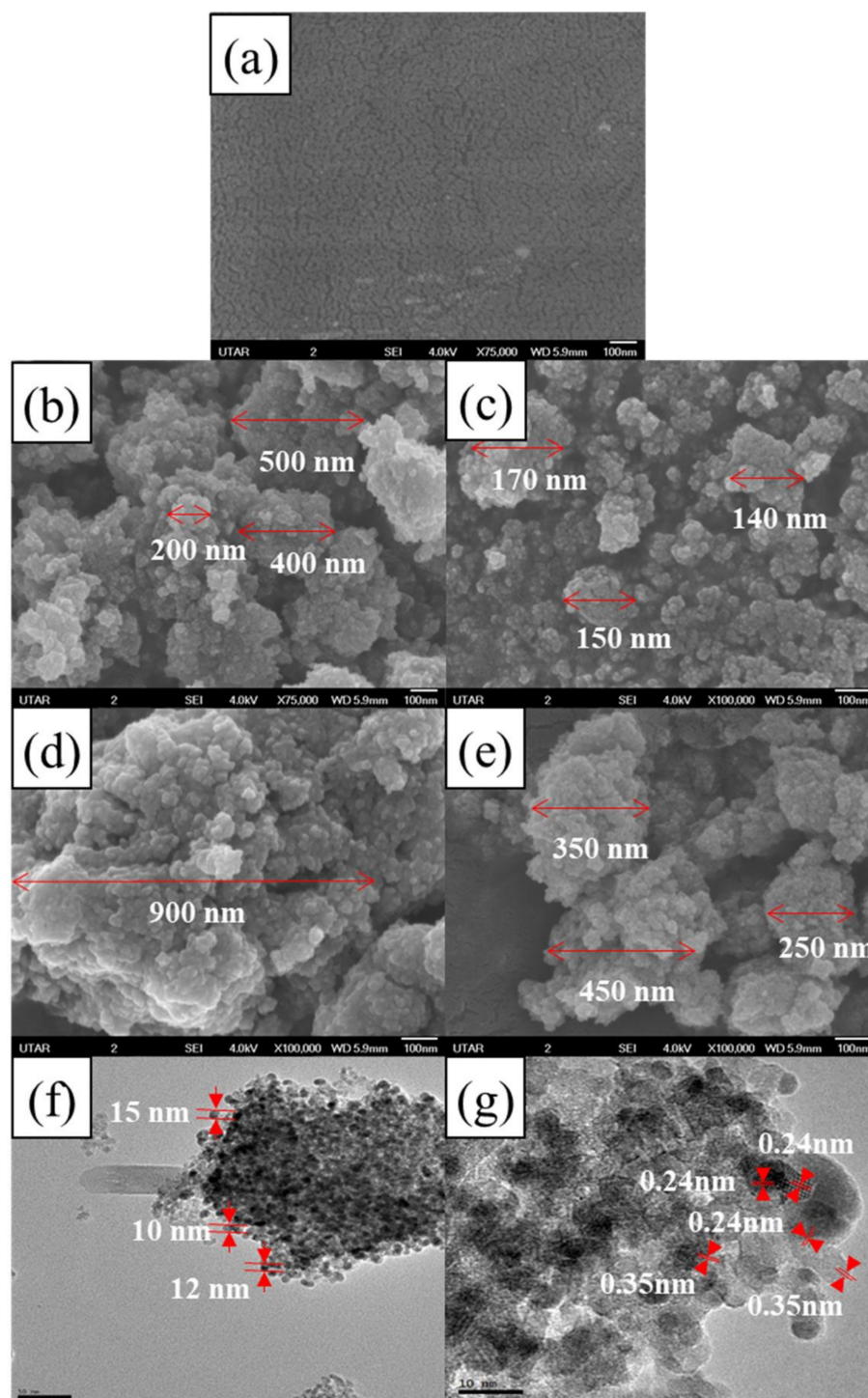**Figure 1.** FESEM images of (**a**) cellulose, (**b**) TiO_2, (**c**) 0.05 cellulose/TiO_2, (**d**) 0.05 Ag/TiO_2, and (**e**) cellulose/Ag/TiO_2; HRTEM images of cellulose/Ag/TiO_2 at magnifications of (**f**) 50,000× and (**g**) 100,000×.

In the past, surfactants (i.e., sodium dodecyl benzene sulfonate, polyvinylpyrrolidone, 1,2,3,4-butanetetracarboxylic acid, poly(methacrylic acid), and hexadecyl trimethyl ammonium bromide) or stabilizers were added to prevent agglomeration and to control the size to achieve good dispersion of TiO_2 nanomaterials [26]. However, rapid nucleation and slow crystal growth were observed when utilizing these surface-active materials. In this study, TiO_2 nanoparticles were distributed on the cellulose by using a simple mixing method to intercalate the unstable TiO_2 nanoparticles. It was anticipated that cellulose served as a carbon support material for the adherence of nanoparticles, which in turn hindered TiO_2 agglomeration/aggregation and increased the dispersity of the nanoparticles, as shown in Figure 1c. A noticeable larger particle size of 0.05 Ag/TiO_2 (>15 nm) was aggregated into a larger cluster of about 900 nm, as shown in Figure 1d. This revealed the strong interaction between Ag/TiO_2 nanoparticles. Barakat et al. [27] also reported a similar result where the introduction of Ag resulted in the formation of larger aggregates of TiO_2 particles. Meanwhile, the incorporation of cellulose into the 0.05 Ag/TiO_2 sample demonstrated smaller aggregated nanoparticles ranging from 250 to 450 nm, as shown in Figure 1e, than compared to 0.05 Ag/TiO_2.

Figure 1f,g show the high-resolution TEM images of cellulose/Ag/TiO_2. The particle size of the cellulose/Ag/TiO_2 was in the range of 10–15 nm and slightly agglomerated, as shown in Figure 1f. No clear lattice fringe can be observed for the cellulose, which suggests their amorphous carbon nature [28]. The localized doping of Ag on the surface of TiO_2 was spotted in Figure 1g. The crystalline lattice fringe spacing of 0.35 nm corresponded to the (101) facet of the anatase phase of TiO_2, while 0.24 nm corresponded to Ag (111) facet. These spacings could be clearly identified, as shown in Figure 1g [29]. These findings were consistent with the results obtained from the XRD analysis.

The EDX analysis was performed to quantitatively evaluate the elements present on the material. Based on the results shown in Table 1, it proved the formation of TiO_2 after hydrothermal processes as the detected atomic ratio of Ti and O (1:2.1) was quite close to the stoichiometric composition of TiO_2. The detected 4.54 wt% Ag element in 0.05 Ag/TiO_2 was close to the actual amount loaded on TiO_2 (5% wt./wt.). Singh et al. [30] reported that cellulose typically exhibited a higher percentage of carbon than compared to oxygen elements. The detected silica indicated that silica bodies were also embedded in the OPEFB fiber, while sodium and chloride elements were contributed by the alkaline treatment followed by acid hydrolysis during the extraction of cellulose.

Table 1. EDX analysis of TiO_2, cellulose, 0.05 cellulose/TiO_2, 0.05 Ag/TiO_2, and cellulose/Ag/TiO_2.

Element/ Samples	TiO_2		Cellulose		0.05 Cellulose/TiO_2		0.05 Ag/TiO_2		Cellulose/Ag/TiO_2	
	Weight %	Atomic %	Weight %	Atomic %	Weight %	Atomic %	Weight %	Atomic %	Weight %	Atomic %
Ti	58.64	32.13	-	-	49.55	23.71	56.41	32.17	42.59	19.60
O	32.13	67.87	46.10	40.03	41.99	60.15	39.05	66.68	40.29	55.52
C	-	-	50.45	58.35	8.46	16.15	-	-	19.60	24.06
Ag	-	-	-	-	-	-	4.54	1.15	4.00	0.82
Si	-	-	0.54	0.27	-	-	-	-	-	-
Na	-	-	0.99	0.60	-	-	-	-	-	-
Cl	-	-	1.93	0.76	-	-	-	-	-	-

3.1.2. XRD

Figure 2 shows the XRD patterns of TiO_2, cellulose, 0.05 cellulose/TiO_2, 0.05 Ag/TiO_2, and cellulose/Ag/TiO_2. The diffraction peaks of anatase TiO_2 displayed at 25.30, 37.88, 47.92, 62.66, 69.22, and 75.27° were attributed to the respective planes of (101), (004), (200), (204), (116), and (215) [31,32]. There were two diffraction peaks of rutile TiO_2 found at 54.47 and 69.78°, which were indexed as (211) and (112) planes, respectively [33]. This demonstrated that the dominant phase was anatase and the minor phase was rutile in the prepared TiO_2. Meanwhile, the diffraction peaks of cellulose appeared at 16.08, 22.26, and

34.63°, which could be contributed to the (101), (002), and (040) crystallographic planes of cellulose I polymorph [20]. Islam et al. [34] reported that the small peak at 34.5° indicated the removal of lignin and hemicellulose after chemical treatment. The results indicated the successful extraction of cellulose from OPEFB.
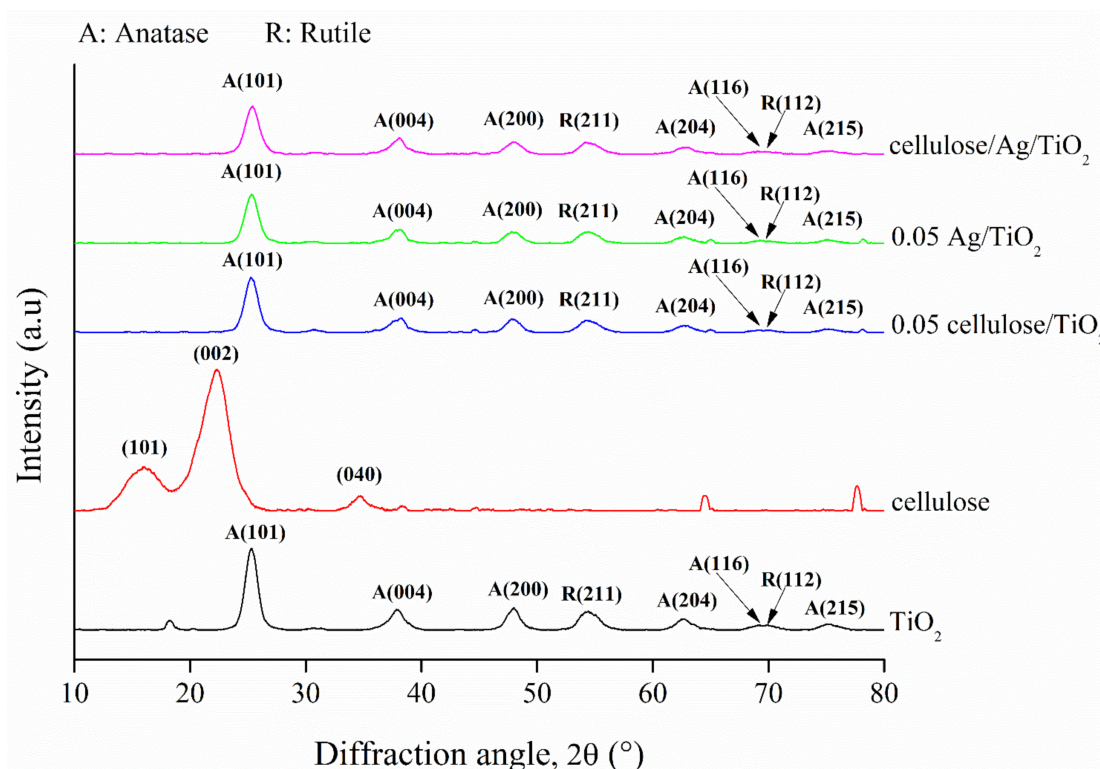

Figure 2. XRD patterns of TiO_2, cellulose, 0.05 cellulose/TiO_2, 0.05 Ag/TiO_2, and cellulose/Ag/TiO_2.

On the other hand, 0.05 cellulose/TiO_2, 0.05 Ag/TiO_2, and cellulose/Ag/TiO_2 displayed similar diffraction peaks as the TiO_2 sample. However, the diffraction peak intensity at 25.30° was reduced after the introduction of foreign substances such as cellulose and Ag into the prepared samples. No Ag characteristic peaks were found in 0.05 Ag/TiO_2 and cellulose/Ag/TiO_2, which may be ascribed to the relatively low Ag content on the surface. Komaraiah et al. [31] reported that lower amount of Ag (<5 at %) would result in a high dispersion of Ag elements on the TiO_2 surface. They claimed that the diffraction signal for metallic Ag at 44.3° would appear only if using a higher amount of Ag doping.

Moreover, the decrement of the peaks intensity was attributed to the reduction in crystallite sizes in both 0.05 Ag/TiO_2 and cellulose/Ag/TiO_2. The average crystallite sizes of the synthesized samples were estimated by using Debye–Scherrer's equation [35]. The crystallite sizes of the TiO_2, 0.05 cellulose/TiO_2, 0.05 Ag/TiO_2, cellulose/Ag/TiO_2, and cellulose were 6.55, 6.49, 5.94, 6.09, and 3.27 nm, respectively. These sizes were in good agreement with the results obtained from FESEM and HRTEM analyses as reported in the earlier section. According to Dey et al. [36], only a limited amount of Ag ions would be incorporated into the TiO_2 lattice due to the larger ionic radius of Ag^+ (0.126 nm) as compared to Ti^{4+} (0.068 nm). The ions would mostly accommodate themselves in the interstitial sites or deposited on the surface of TiO_2.

3.1.3. FTIR Analysis

Figure 3 shows the FTIR spectra for TiO_2, cellulose, 0.05 cellulose/TiO_2, 0.05 Ag/TiO_2, and cellulose/Ag/TiO_2. The broad peak between 400 cm^{-1} and 1000 cm^{-1} found in the pure TiO_2 and TiO_2-based samples was due to the stretching vibrations of Ti–O, Ti–O–C, and Ti–O–Ti bonds in the TiO_2 lattice structure [37]. This implied the formation of Ti-OH bonds in all these samples.
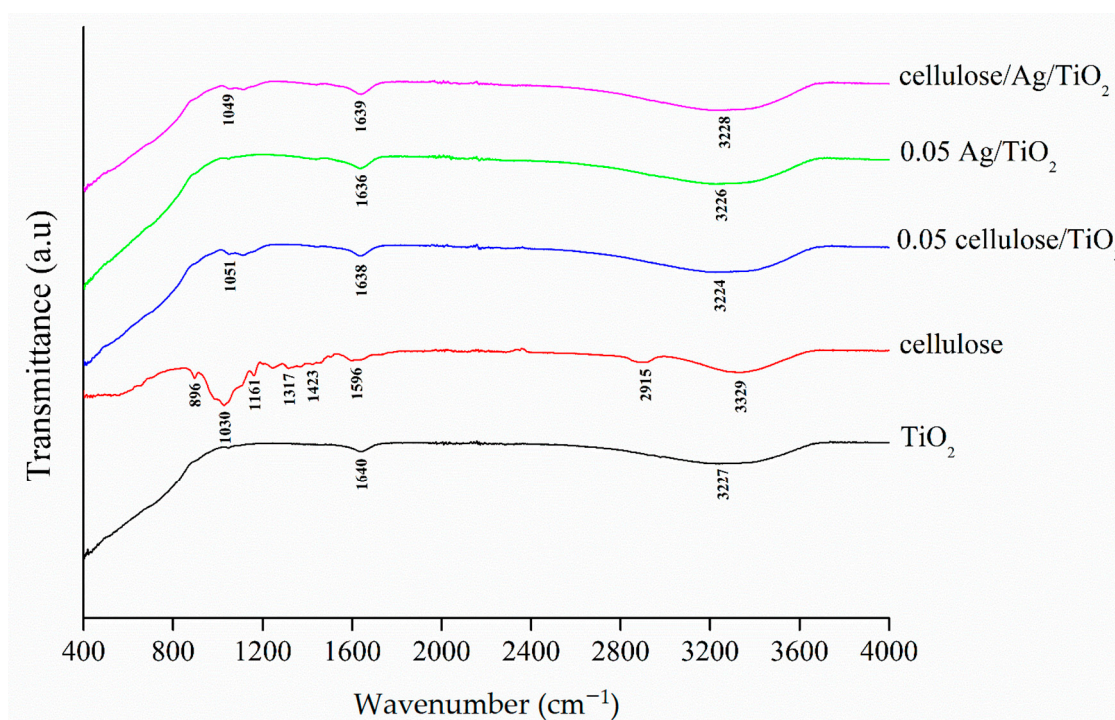
Figure 3. FTIR spectra of TiO_2, cellulose, 0.05 cellulose/TiO_2, 0.05 Ag/TiO_2, and cellulose/Ag/TiO_2.

Cellulose exhibited characteristic bands at 896 cm^{-1}, 1030 cm^{-1}, 1161 cm^{-1}, 1317 cm^{-1}, 1423 cm^{-1}, and 2915 cm^{-1}, which corresponded to the β-glucosidic linkages between the glucose monomers, stretching vibration of C–O–C within saccharide rings, asymmetric valence vibrations of C–O–C, bending of C–H, bending vibration of –CH$_2$, and stretching vibration of C–H bonds, respectively [38,39]. All these characteristic bands corresponded to cellulose I [38,39]. The peak shifting from 1030 cm^{-1} to 1051 cm^{-1} and 1049 cm^{-1} found in 0.05 cellulose/TiO_2 and cellulose/Ag/TiO_2, respectively, indicated the bonding interaction between cellulose and TiO_2 where the stretching vibration of C–O–C within saccharide rings was present.

Meanwhile, the two peaks around 3440 cm^{-1} and 1630 cm^{-1} observed in all samples were ascribed to the stretching vibration of hydroxyl groups (−OH) and adsorbed water molecules on the surface of samples, which was also reported in previous literature [40]. Both high intensity peaks at 3329 cm^{-1} and 1596 cm^{-1} found in cellulose indicated the presence of high density free hydroxyl groups and water molecules that adsorbed onto the cellulose after the removal of lignin and hemicellulose from the surface of the fibers [41]. The addition of cellulose and/or Ag into TiO_2 increased the peaks intensity, which was related to the water molecules adsorbed by the composite materials. It should be highlighted that the presence of OH groups is beneficial for generating ●OH radicals during the sonocatalysis process.

3.1.4. Surface Analysis

Nitrogen adsorption–desorption isotherms were conducted to further illustrate the porosity structure of all the prepared samples. Figure 4 shows the nitrogen adsorption–desorption isotherms and pore size distributions of the samples. According to IUPAC classification [42], all samples exhibited type IV isotherms with H3 hysteresis loops, indicating the slit-like shape mesoporous characteristics of materials (2–50 nm). The dramatic increase in nitrogen adsorption at high relative pressures (above P/P_0 = 0.6) indicated the changes of monolayer to multilayer adsorption of nitrogen followed by capillary condensation inside the mesopores [39]. The multilayer adsorption and capillary condensation happened at higher relative pressures (P/P_0 = 0.6–0.99) further confirmed the presence of uniform mesopores, which covered the surface of TiO_2, 0.05 cellulose/TiO_2, 0.05 Ag/TiO_2,

and cellulose/Ag/TiO$_2$. This was consistent with previous studies regarding TiO$_2$ hybrid samples [43]. Alothman [44] reported that the desorption curve of H3 hysteresis consisted of a slope-related force on the hysteresis loop due to the tensile strength effect that might occur for nitrogen at 77 K and the relative pressure range of 0.4–0.45. Cellulose exhibited a horizontal trend of nitrogen adsorption and desorption at relative pressures between 0.2 and 0.9, which revealed a relatively lower external surface area [45]. Further evidence could be found from the pore size distribution shown in Figure 4b. Its external surface area was mainly constituted in the macropores regions. This feature could limit the adsorption capacity of cellulose during the adsorption followed by oxidation process. A similar low specific surface area of pristine cow dung (0.7456 m^2/g) was also being reported by Zhu et al. [46].
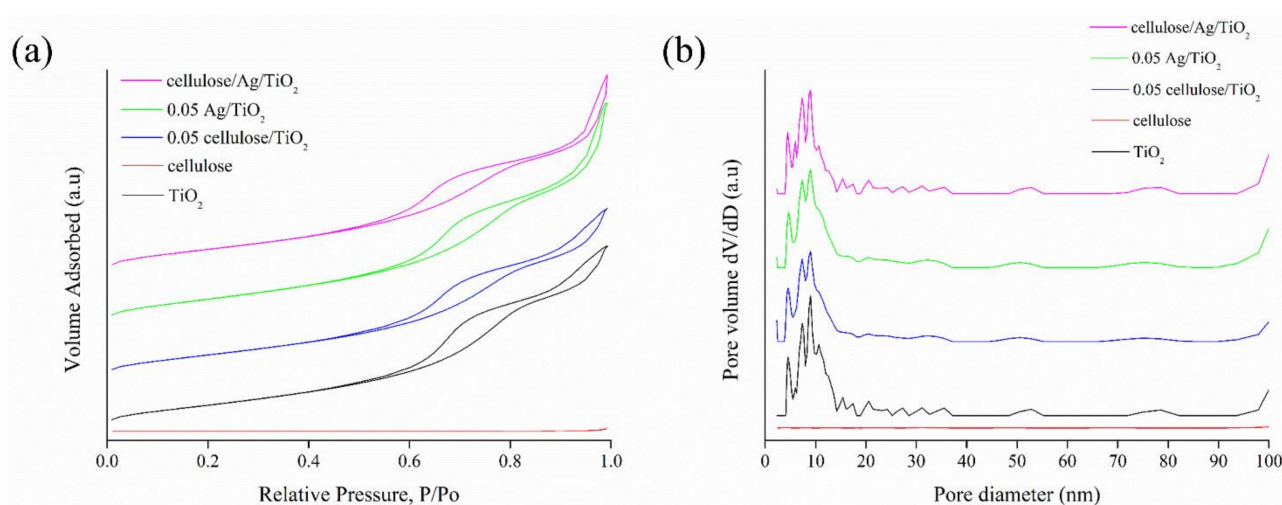

Figure 4. (**a**) Nitrogen adsorption–desorption plot and (**b**) pore size distribution of TiO$_2$, cellulose, 0.05 cellulose/TiO$_2$, 0.05 Ag/TiO$_2$, and cellulose/Ag/TiO$_2$.

Figure 4b shows the pore size distribution curves of the samples. It was observed that all samples exhibited wide mesopore sizes ranging from 3 to 50 nm. Based on Table 2, the average pore size of TiO$_2$, cellulose, 0.05 cellulose/TiO$_2$, 0.05 Ag/TiO$_2$, and cellulose/Ag/TiO$_2$ were 7.58, 26.45, 7.38, 8.83, and 8.41 nm, respectively. It was reported that mesoporous structure was beneficial for catalytic process due to its short bulk diffusion length of charge carriers and transport pathways for the diffusion of reactants [47].

Table 2. Surface analysis of TiO$_2$, cellulose, 0.05 cellulose/TiO$_2$, 0.05 Ag/TiO$_2$, and cellulose/Ag/TiO$_2$.

Sample	Pore Size (nm)	Pore Volume (cm^3/g)	Specific Surface Area (m^2/g)
TiO$_2$	7.58	0.3287	146.46
cellulose	26.45	0.0038	0.88
0.05 cellulose/TiO$_2$	7.38	0.3043	142.06
0.05 Ag/TiO$_2$	8.83	0.3828	157.58
cellulose/Ag/TiO$_2$	8.41	0.3251	150.22

As shown in Table 2, 0.05 Ag/TiO$_2$ and cellulose/Ag/TiO$_2$ nanocomposites had higher specific surface area and pore size than pure TiO$_2$. Interestingly, the surface area of 0.05 Ag/TiO$_2$ was substantially higher than that of TiO$_2$, as shown in Table 2. This indicated that Ag not only served as the plasmonic light absorber but also enhanced the surface area contributed by the decrement of nanoparticles sizes of the tetragonal phase of TiO$_2$ at an appropriate dopant amount [48]. The high surface area usually favors the

reaction due to the presence of more active sites that can enhance the catalytic activities. It is worth noting that the surface area of cellulose/Ag/TiO$_2$ decreased slightly after the incorporation of cellulose. The decrease in surface area of cellulose/Ag/TiO$_2$ could be caused by blockages and coverage of cellulose on the adsorption/active sites of Ag/TiO$_2$. Nevertheless, Ng and Leo [39] mentioned that cellulose could promote the dispersion of Ag/TiO$_2$ nanoparticles and helped to reduce particle agglomeration without affecting the specific surface area.

It was reported that large BET surface area was beneficial for the dispersion of active species (i.e., low valance Ti species and oxygen vacancies) and allowed higher exposure to the organic dye adsorption followed by oxidation [49]. The larger mesopores would also accelerate the diffusion of reactants and products, which contributed to higher catalytic performance. The incorporation of Ag nanoparticles also contributed to the growth of pore size and pore volume in 0.05 Ag/TiO$_2$ and cellulose/Ag/TiO$_2$. The formation of larger mesopores pore size, pore volume, and specific surface area of cellulose/Ag/TiO$_2$ was expected to promote the performance of cellulose/Ag/TiO$_2$ during the degradation of dye pollutants.

There was also a slight decrease in the specific surface area, pore size, and pore volume of 0.05 cellulose/TiO$_2$ with respect to the bare TiO$_2$ counterpart. Oliveira et al. [50] reported a similar decrement in surface area for cellulose-TiO$_2$ hybrids at various cellulose loadings. They claimed that it might be related to the partial blockage of the mesopore structure in TiO$_2$ by the cellulose entities.

3.1.5. Optical Properties

The optical properties of TiO$_2$, cellulose, 0.05 cellulose/TiO$_2$, 0.05 Ag/TiO$_2$, and cellulose/Ag/TiO$_2$ were determined using UV–Vis DRS, and the results are shown in Figure 5a. TiO$_2$ showed absorption in the ultraviolet (UV) region (200 to 400 nm) and absorption edge at approximately 400 nm due to the intrinsic band gap transition from the valence band to the conduction band of TiO$_2$ and the existence of rutile phase [51,52]. Meanwhile, 0.05 cellulose/TiO$_2$, 0.05 Ag/TiO$_2$, and cellulose/Ag/TiO$_2$ showed higher absorption properties due to the Schottky heterojunction formed between Ag or cellulose and TiO$_2$ [52]. The optical absorption edge for TiO$_2$-based materials was shifted from the UV range into visible range (i.e., red shift) of cellulose/Ag/TiO$_2$, which implied the synergistically effect of the Ag or cellulose material that enhanced the absorption of visible light. Yang and Luo [51] reported that the extension of visible light absorption to above 500 nm might be due to the local surface plasmon resonance effect of the metallic species. They also claimed that Ag nanoparticles could induce TiO$_2$ valence band edges to absorb visible light.
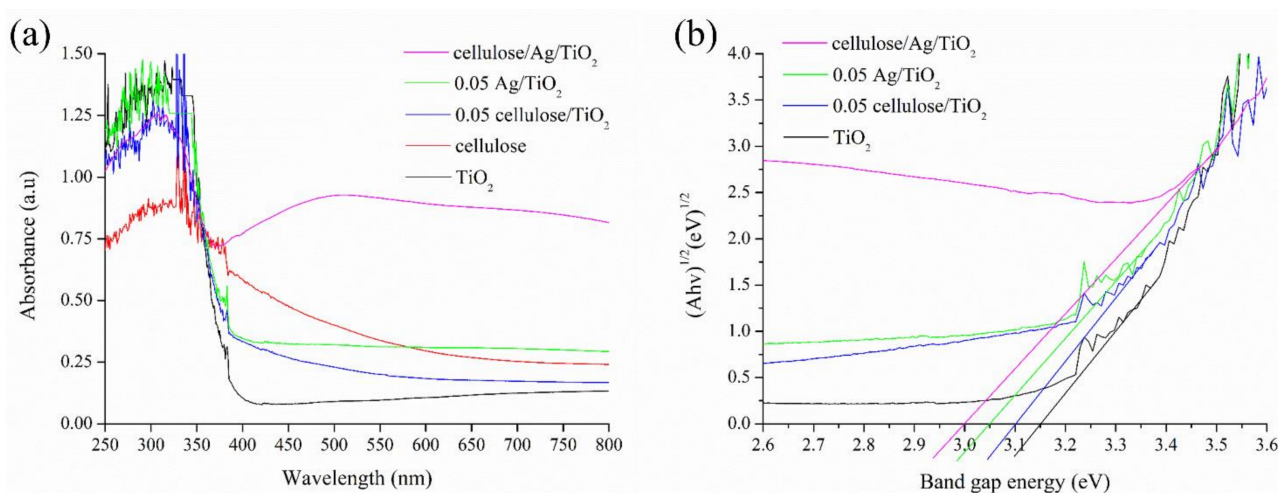

Figure 5. (**a**) Optical properties and (**b**) band gap energy of the prepared samples.

This red shift of light absorption suggested a decrement in the band gap energy as shown in Figure 5a. The band gap energies of the prepared samples were determined by employing the Tauc's plot, as shown in Equation (2) [40]:

$$\alpha h\nu = A\left(h\nu - E_g\right)^{n/2} \tag{2}$$

where $h\nu$ is the incident photon energy, α is the absorption coefficient, A is a constant, and E_g is the band gap energy (eV). The value of $n = 4$ represents the indirect transition. Figure 5b presents the plots of $(Ah\nu)^{1/2}$ versus band gap energy. The E_g values of TiO_2, 0.05 cellulose/TiO_2, 0.05 Ag/TiO_2, and cellulose/Ag/TiO_2 were about 3.15, 3.1, 3.05, and 3 eV, respectively. Xue et al. [53] claimed that the lower band gap energies of nanocomposite samples than compared to bare TiO_2 were due to the surface plasmon effect of Ag^0. Zhou et al. [40] reported that the formation of Schottky junction at the interface of Ag nanoparticles and TiO_2 could capture the generated electrons and resulted in the accumulation of redundant electrons on Ag nanoparticles. This inhibited the recombination rate of electron-hole pairs and, subsequently, enhanced light response and catalytic activity. The lower band gap energies findings confirmed the enhancement of light utilization efficiency for the nanocomposite materials.

3.1.6. PL

Photoluminescence (PL) measurements were performed to study the radiative recombination of photo-induced electrons and holes that emit fluorescence, and the results are shown in Figure 6. High PL intensity usually denotes a strong recombination rate of charge carriers and vice versa. The irregular shapes of the PL spectrum for TiO_2 indicated that the sample exhibited several emission peaks. The PL bands might be assigned to the conductor and valence bands transition (399 nm) [54], the free excitons of band edge (450 nm) [55], surface oxygen vacancies associated with Ti^{3+} in anatase (438, 490, 540, and 606 nm) [31,55], the crystal lattice defects (480 nm) [55], recombination of the photo-induced electron–hole pair (468 nm) [55], and the transition between the gap state and valence band (620 nm) [54].
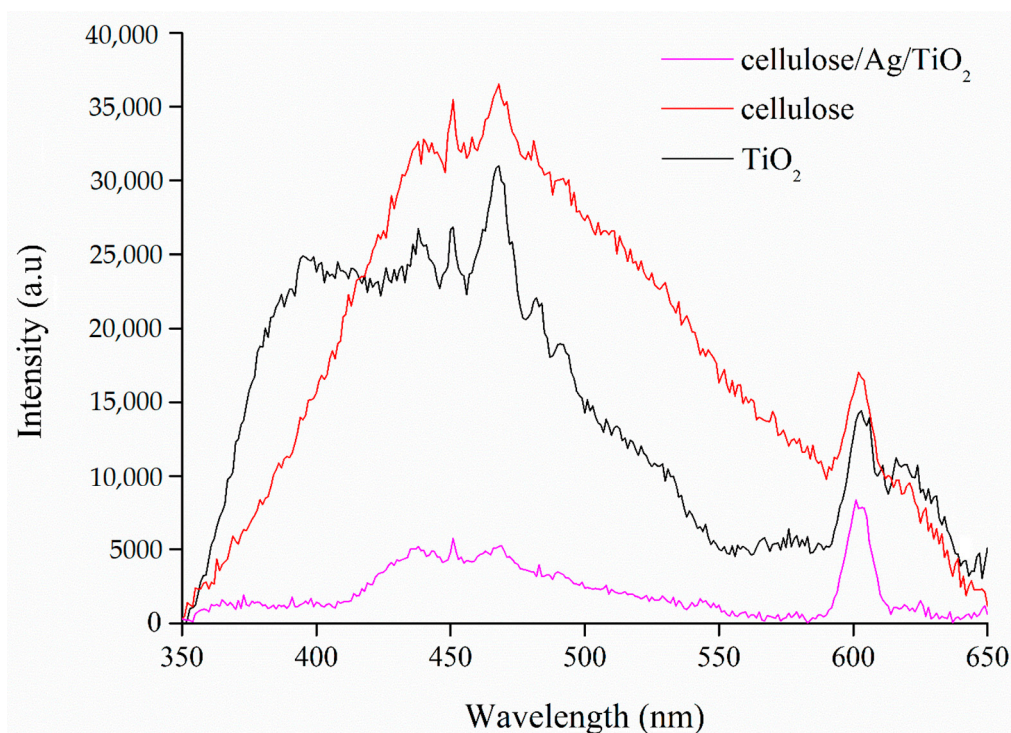

Figure 6. PL spectra of TiO_2, cellulose, and cellulose/Ag/TiO_2.

As shown in Figure 6, the fluorescence emission spectrum of cellulose exhibited emission peaks at about 440, 481, and 602 nm when excited at 300 nm. Liu et al. [56] reported that the unique emission behaviors of cellulose may originate from the electron-rich oxygen and/or glucose units, which also confirms the aggregation-induced or crystallization-induced emissions from cellulose. Shanthini et al. [57] also revealed that cellulose consisted of two intense PL bands at about 420–440 nm and 480–490 nm. On the other hand, the decreasing PL intensity in cellulose/Ag/TiO$_2$ was attributed to a decrease in the recombination rate of charge carriers in TiO$_2$ and the improvement of charge separation. Mahnae et al. [58] reported that Ag nanoparticles could act as surface trap centers for emitting electrons, and this could decrease the PL intensity of cellulose/Ag/TiO$_2$. Consequently, generated electrons and holes in TiO$_2$ had a high probability to react with oxygen and water molecules, respectively, to produce highly reactive oxygen species that were capable in degrading organic pollutants via oxidation processes, as highlighted by Sboui et al. [59].

3.1.7. XPS

XPS analysis was employed to detect the elemental composition and chemical states in cellulose/Ag/TiO$_2$. The wide scanning XPS spectrum shown in Figure 7a demonstrated that the surface elemental composition for cellulose/Ag/TiO$_2$ comprised 25.71% Ti, 61.02% O, 12.22% C, and 1.05% Ag. Figure 7b shows the high-resolution XPS spectra of the Ti 2p and the two characteristic peaks located at binding energies of 459.6 and 465.3 eV. They were corresponded to Ti 2p$_{3/2}$ and Ti 2p$_{1/2}$, which were in agreement with the reported literature data for the anatase phase [60,61]. The obtained energy difference of 5.7 eV in the Ti 2p doublet due to spin-orbit splitting also confirmed the existence of Ti^{4+} species in TiO$_2$ [62].
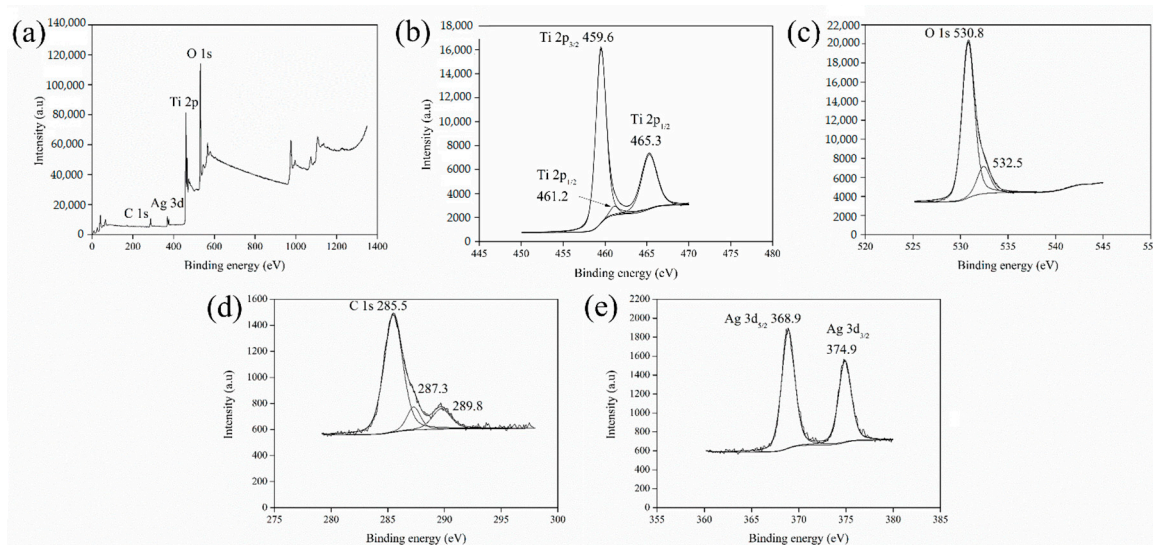

Figure 7. XPS spectra of cellulose/Ag/TiO$_2$: (**a**) survey, (**b**) Ti 2p peaks, (**c**) O 1s peaks, (**d**) C 1s peaks, and (**e**) Ag 3d peaks.

A weak Ti 2p$_{1/2}$ peak located at 461.2 eV might be attributed to the Ti^{3+} sites in TiO$_2$ lattice, which indirectly demonstrated the presence of oxygen vacancies [63]. The abundant hydroxyl groups in cellulose played an important role in the reduction of Ti^{4+} to Ti^{3+} during the hydrothermal process [64]. Fu et al. [65] reported that the C-OH in the alcohol (i.e., ethanol and isopropanol) from the hydrolysis of titanium isopropoxide could reduce Ti^{4+} to Ti^{3+}. On the other hand, Wang et al. [66] reported that the minority of Ti^{3+} species (Ti^{3+} 2p$_{1/2}$ and 2p$_{3/2}$) might be related to a redox reaction involved in TiO$_2$ and monovalent Ag(I) species, Ag$^+$ + Ti^{3+} → Ag^0 + Ti^{4+}. It was reported that the Ti^{3+} and oxygen vacancies could build a new energy level and hinder the recombination of electrons and holes [67]. The oxygen vacancy sites were more likely to adsorb oxygen molecules to form chemisorbed oxygen species, such as superoxide radicals (O^{2-}).

In the O1s spectrum shown in Figure 7c, the two peaks formed at binding energies of 530.8 and 532.5 eV were associated with the lattice oxygen in TiO_2 (O–Ti–O bond) and chemisorbed water molecules or carbonyl groups from cellulose (Ti–O–H or Ti–O–C), respectively [41,59]. The surface adsorbed oxygen would react with the generated electrons to produce anion radicals. Meanwhile, the reactive and unstable –OH groups would react with the generated holes to produce ●OH radicals [68].

Figure 7d shows the high-resolution XPS spectrum of C 1s in cellulose/Ag/TiO_2, which exhibits three splitting peaks at 285.5, 287.3, and 289.8 eV. The carbon peak located at 285.5 eV was attributed to the C–C or C–H bonds originating from a surface layer of adventitious carbon [69,70]. The carbon peak occurred at 287.3 eV was associated with the O–C–O or C–OH bonds [71,72]. Another carbon peak formed at 289.8 eV was attributed to carbonyl, aldehydic, or ketonic carbon on the surface of cellulose/Ag/TiO_2 [41]. This peak at 289.8 eV was also associated with the carboxylic or carbonate groups generally present on the surface of the metal oxides [51,73].

The high-resolution XPS spectrum of Ag 3D region peaked at 368.9 and 374.9 eV, as shown in Figure 7e. The binding energies of 368.9 and 374.9 eV corresponded to Ag $3d_{5/2}$ and Ag $3d_{3/2}$, respectively [74]. The obtained 6 eV of energy spacing between these two peaks confirmed the characteristics of Ag nanoparticle whereby Ag existed in the form of Ag^0 [75]. The presence of Ag^0 indicated that the Ag ions were reduced to Ag atoms in cellulose/Ag/TiO_2.

3.2. Catalytic Performance

The sonocatalytic activities of different mass ratios of cellulose/TiO_2 were studied, and the results are shown in Figure 8a. It was found that the sonocatalytic degradation efficiency of Congo red was extremely slow and negligible (4.3% after 60 min) in the presence of cellulose alone. The sonocatalytic degradation efficiency of Congo red increased to 48.3% when utilizing an appropriate amount of cellulose incorporated into TiO_2 (0.05 cellulose/TiO_2). A decreasing trend in the sonocatalytic performance of Congo red was observed when increasing the amount of cellulose beyond the optimum mass ratio value. This might be related to the increasing contact area and surface exposition of cellulose entities in cellulose/TiO_2 [50]. The surface adsorption sites for dye molecules on cellulose allowed the neighboring TiO_2 to interact with the adsorbed dye molecules easily. This subsequently facilitated their interactions with the generated electrons-holes carriers for oxidation process to occur. Although 0.05 cellulose/TiO_2 exhibited slightly lower surface area value (142.06 m^2/g) than compared to TiO_2 (146.46 m^2/g), its interfaced network and abundant –OH groups endowed within 0.05 cellulose/TiO_2 served as a better catalyst compared to TiO_2 itself.

Voisin et al. [76] reported that the excellent adsorption properties of nanocellulose for various pollutants could contribute to the high catalytic activity of the hybrid materials by trapping the dye molecules close to the active centers. Based on the XRD analysis, the average crystallite size of 0.05 cellulose/TiO_2 (6.49 nm) was smaller than pure TiO_2 (6.55 nm). Nsib et al. [77] reported that the small crystallite size could give rise to a large number of small particles, which acted as reactive sites for the reaction of the holes with the H_2O and –OH groups adsorbed at the TiO_2 surface to generate ●OH radicals. Moreover, the formation of organic–inorganic inter-penetrating networks could also create more –OH groups on the cellulose surface and contribute to the formation of more ●OH radicals than compared to bare TiO_2. These ●OH radicals produced by the 0.05 cellulose/TiO_2 composite were important for reacting with the adsorbed dye molecules and formed lower molecular weight degradation products.
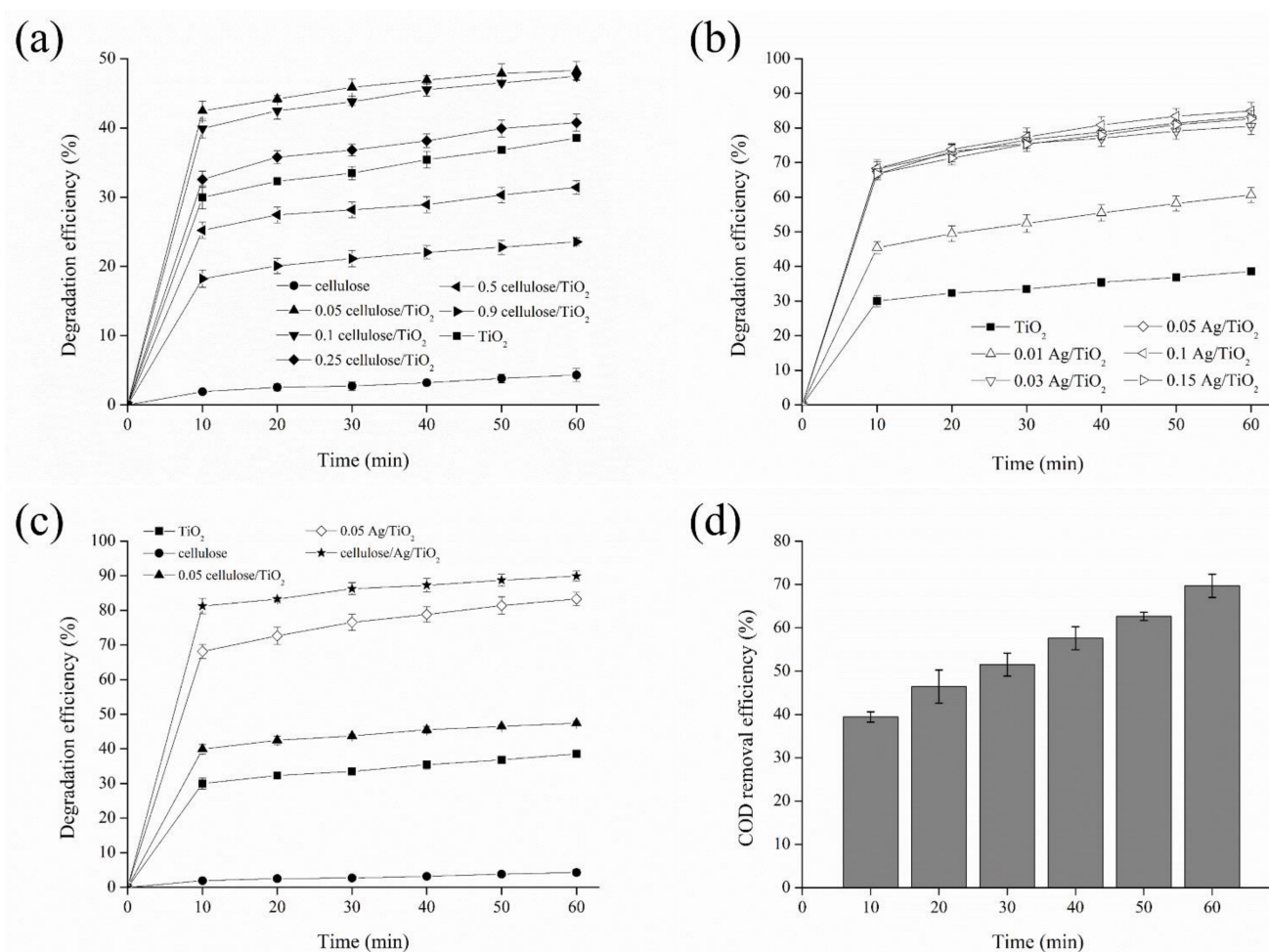
Figure 8. Degradation efficiency of Congo red for (**a**) cellulose/TiO$_2$ composites, (**b**) Ag/TiO$_2$ composites, (**c**) cellulose /Ag/TiO$_2$, and their (**d**) COD removal efficiencies under ultrasonic irradiation (initial dye concentration = 10 mg/L, catalyst loading = 0.5 g/L, treatment time = 60 min, ultrasonic frequency = 24 kHz, and power = 280 W).

Figure 8b shows the effect of different mass ratio of Ag/TiO$_2$ on the sonocatalytic degradation efficiency of Congo red. The sonocatalytic degradation efficiency of Congo red initially increased from 60.7% to 80.5% when increasing the mass ratio of Ag: TiO$_2$ from 0.01:1 to 0.03:1. The sonocatalytic performance only increased insignificantly when further increasing the mass ratio of Ag: TiO$_2$ to 0.1:1. An appropriate amount of Ag nanoparticles could enhance the catalytic performance of TiO$_2$ through charge transferring, electron trapping, and reduction in band gap energy [78]. Yang and Luo [51] reported that an excessive amount of Ag metal might form a charge trapping center for electron-hole pairs, restrain the movement of charge carriers, and consequently reduce catalytic efficiency. Although 0.1 Ag/TiO$_2$ achieved the highest sonocatalytic performance among the Ag-doped TiO$_2$ samples, 0.05 Ag/TiO$_2$ (83.3%) with the catalytic performance close to 0.1 Ag/TiO$_2$ (84.9%) was selected for the subsequent study after considering the lower impact on catalyst development cost.

Figure 8c shows the sonocatalytic degradation efficiency of Congo red in the presence of various types of catalysts. The results showed the insignificant sonocatalyic degradation of Congo red in the presence of cellulose. Lan et al. [79] reported that cellulose has no capability of absorbing the visible light and showed insignificant absorption of UV light (<250 nm). Meanwhile, the sonocatalytic degradation efficiency of Congo red in the presence of cellulose/Ag/TiO$_2$ significantly increased to 89.9%. Ahmadi et al. [3] reported that the small particle size of the catalyst could increase the surface area available for degradation of organic pollutants. The smaller particle size and larger specific surface area

found in cellulose/Ag/TiO$_2$ than compared to other types of catalysts provided additional active sites, which promoted the mass transfer of dye pollutants between the liquid and the catalyst surface. The synergistic effect between Ag, cellulose, and TiO$_2$ nanoparticles might be related to the generation of numerous •OH radicals that promoted electron transfer ability, the reduction in recombination rate of charge carriers, and the decrease in band gap energy in cellulose/Ag/TiO$_2$. Subsequently, the sonocatalytic performance of Congo red improved by 51.4% in the presence of cellulose/Ag/TiO$_2$ than compared to bare TiO$_2$. Therefore, cellulose/Ag/TiO$_2$ was determined as a suitable catalyst to effectively degrade Congo red under ultrasonic irradiation.

The high degradation efficiency of Congo red was insufficient to indicate the high mineralization of Congo red dye molecules into the final products of carbon dioxide and water. COD analysis is necessary to study the mineralization of Congo red. Figure 8d shows the COD removal efficiency of Congo red in the presence of cellulose/Ag/TiO$_2$. It was found that the COD removal efficiency of Congo red was 39.4% at the first 10 min and eventually increased to 69.7% after ultrasonication for 60 min. The increasing trend in COD removal efficiency was due to the formation of reactive free radicals that promoted the redox reactions for Congo red degradation during ultrasonic irradiation. Compared to degradation efficiency, a lower COD removal efficiency of Congo red indicated that the intermediate organic byproducts remained in the treated solution and mineralization was incomplete. The low mineralization of Congo red might also be related to the degraded aromatic related molecules that inhibited Congo red from being adsorbed onto the surface of cellulose/Ag/TiO$_2$ during ultrasonic irradiation [80].

In order to evaluate the performance of sonocatalytic degradation of Congo red using cellulose/Ag/TiO$_2$, the obtained results were compared with those reported in the literature and shown in Table 3. The obtained results demonstrated that sonocatalytic degradation of 10 mg/L of Congo red in the presence of cellulose/Ag/TiO$_2$ achieved 81.2% in a shorter time period of 10 min. This concluded that the performance of cellulose/Ag/TiO$_2$ at relatively lower catalyst amounts used in this study significantly surpassed those cited in the literature in terms of sonocatalytic degradation efficiency.

Table 3. Comparison of cellulose/Ag/TiO$_2$ performance with other methods for sonocatalytic degradation of Congo Red.

Type of Catalyst	Concentration (mg/L)	Catalyst Loading (g/L)	Ultrasound Power (W)	Treatment Time (min)	Degradation (%)	Ref
KNbO$_3$	5	1.0	300	300	69.23	[81]
TiO$_2$	10	1.0	50	120	25.69	[82]
TiO$_2$	10	1.5	50	180	100	[83]
SnO$_2$/CdSe/Bi$_2$O$_3$	10	1.0	300	150	100	[84]
cellulose/Ag/TiO$_2$	10	0.5	280	10 / 60	81.2 / 89.9	Present work

3.3. Sonocatalytic Degradation Mechanisms of Congo Red

Figure 9 shows the proposed degradation mechanism of Congo red in the presence of cellulose/Ag/TiO$_2$ upon ultrasonic irradiation. Firstly, ultrasonic irradiation is introduced to the Congo red solution in the presence of cellulose/Ag/TiO$_2$. Ultrasonic irradiation triggered the formation of cavitation bubbles [85]. During ultrasonic irradiation, cellulose/Ag/TiO$_2$ nanoparticles imparted more nucleation sites and increased the occurrence of cavitation bubbles [86]. These bubbles subsequently underwent formation, oscillation, growth, and finally collapsed. When the cavitation bubbles collapsed, the large amount of energy released would generate instantaneous hot spots with high temperature and pressure. These hot spots facilitated the thermal dissociation of water and oxygen

by producing •OH and H$^+$ radicals (Equation (3)) [3]. These free radicals consisted of unpaired electrons that were highly reactive and possessed strong oxidation abilities [85].
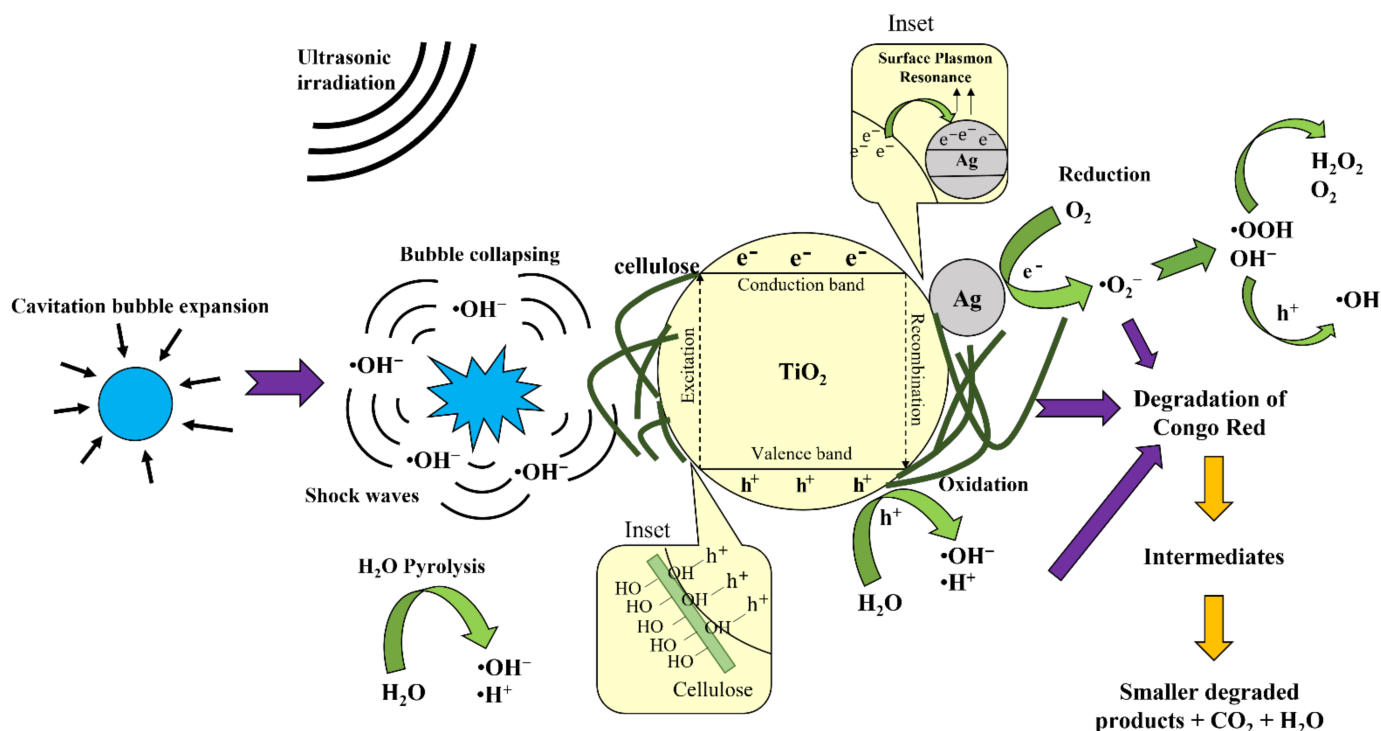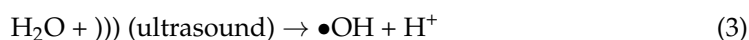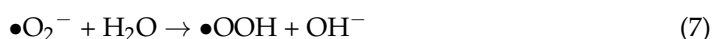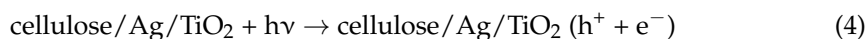
$$H_2O +))) \text{ (ultrasound)} \rightarrow •OH + H^+ \tag{3}$$

Figure 9. Proposed sonocatalytic degradation mechanism of Congo red with cellulose/Ag/TiO$_2$.

Meanwhile, sonoluminescence occurred during the collapse of cavitation bubbles and emitted an instantaneous flash of light [87]. This flash light was able to excite electrons from the conduction band and left holes at the valence band of TiO$_2$ (Equation (4)) [86]. The generated electrons reduced the oxygen molecules to form superoxide (•O$_2^-$) radicals (Equation (5)), while the generated holes (h$^+$) oxidized the water molecules to form •OH radicals (Equation (6)). The generated •O$_2^-$ radicals further reacted with the water molecules to form hydroperoxyl (•OOH) radicals and hydroxide (OH$^-$) ions, which resulted in the production of hydrogen peroxide (H$_2$O$_2$) molecules (Equations (7)–(8)) [51]. The reaction of OH$^-$ ions with the generated holes formed •OH radicals (Equation (9)).

$$\text{cellulose/Ag/TiO}_2 + h\nu \rightarrow \text{cellulose/Ag/TiO}_2 \ (h^+ + e^-) \tag{4}$$

$$O_2 + e^- \rightarrow •O_2^- \tag{5}$$

$$H_2O + h^+ \rightarrow •OH + H^+ \tag{6}$$

$$•O_2^- + H_2O \rightarrow •OOH + OH^- \tag{7}$$

$$2•OOH \rightarrow H_2O_2 + O_2 \tag{8}$$

$$OH^- + h^+ \rightarrow •OH \tag{9}$$

The Schottky barrier was created on the Ag/TiO$_2$ interface due to the lower Fermi level of Ag than compared to the conduction band of TiO$_2$, where the conduction band edge positions for TiO$_2$ and Ag were estimated to be -0.11 V and $+0.16$ V vs. SHE, respectively [88]. Such close contact between TiO$_2$ and Ag in the Ag/TiO$_2$ formed the Fermi level alignment to realize a p-n-type heterojunction. Upon excitation, the generated electrons would transfer from conduction band TiO$_2$ to the Ag particles. The conduction band of

Ag nanoparticles served as a trap center for the generated electrons and inhibited the electron-hole recombination rate. Another possible reason was related to the localized surface plasmon resonance effect in Ag nanoparticles, which enabled sonoluminescence light absorption by localized surface plasmon excitation [20]. This would generate electrons and occupy energy levels above the Fermi level of the Ag, thereby restraining the recombination of generated electron-hole pairs onto the surface of TiO_2 [15]. Thus, both electrons from surface plasmon resonance excited Ag nanoparticles and the electrons transferred from TiO_2 to Ag might be captured by the adsorbed O_2 on the catalyst surface to form radical superoxide anions. Subsequently, more reactive radicals were formed to accelerate and oxidize Congo red to intermediate organic byproducts and, finally, into carbon dioxide and water.

Meanwhile, cellulose played an important role in cellulose/Ag/TiO_2 composite during sonocatalysis reaction even though it did not possess any catalytic degradation ability. Innumerable –OH groups existing on the cellulose surface would improve the adsorption capacity in Congo red pollutants removal and captured the holes upon light excitation of TiO_2. Eventually, the electron and hole pairs could be separated, and the reaction between holes and –OH groups would generate ●OH radicals, which was beneficial for the subsequent oxidation reactions in the mineralization process of Congo red. Moreover, Yang and Luo [51] also found that the carbon sites in cellulose behaved similarly to an electron acceptor center for trapping the electrons emitted from the conduction band of TiO_2 and eventually enhanced charge separation efficiency. These generated electrons would migrate to the surface of the particles to undergo reduction processes and produced reactive species such as superoxide ions, which stimulated the radical chain reactions. In short, cellulose was able to assist in the separation of electrons and holes in cellulose/Ag/TiO_2 composites and achieved a high participation rate of charge carriers in the sonocatalytic reaction.

4. Conclusions

In the present work, cellulose/Ag/TiO_2 with the mass ratio of cellulose: Ag: TiO_2 = 0.05:0.05:1 was successfully prepared through the incorporation of OPEFB-derived cellulose on Ag-doped TiO_2 via hydrothermal synthesis. The physicochemical properties of TiO_2, 0.05 cellulose/TiO_2, 0.05 Ag/TiO_2, and cellulose/Ag/TiO_2 were studied through FESEM, EDX, HRTEM, XRD, FTIR, UV–Vis DRS, PL, XPS, and surface analysis. The spherical morphology was not affected in TiO_2-based samples upon preparation. The OPEFB-derived cellulose exhibited cellulose I structure, whereas bare TiO_2 and TiO_2-based samples displayed major anatase and minor rutile phases. The band gap energy and recombination rate of charge carriers in TiO_2 was significantly reduced due to Ag doping. Improvements of the surface properties of cellulose/Ag/TiO_2 such as large mesopores pore size, pore volume, and specific surface area promoted the sonocatalytic performance of cellulose/Ag/TiO_2. The sonocatalytic degradation efficiency of Congo red successfully achieved 89.9% in the presence of cellulose/Ag/TiO_2 at optimum conditions (catalyst loading = 0.5 g/L, initial dye concentration = 10 mg/L, treatment time = 60 min, ultrasonic frequency = 24 kHz, and power = 280 W). The synergetic effect of cellulose improved the catalytic activity of Ag/TiO_2, which prolonged the lifetime of the hole and electron pairs to participate in redox reactions. This study has proven the usefulness of biomass-derived cellulose in the development of an efficient sonocatalyst.

References

1. Serrano-Martínez, A.; Mercader-Ros, M.T.; Martínez-Alcalá, I.; Lucas-Abellán, C.; Gabaldón-Hernández, J.A.; Gómez-López, V.M. Degradation and toxicity evaluation of azo dye Direct red 83:1 by an advanced oxidation process driven by pulsed light. *J. Water Process. Eng.* **2020**, *37*, 101530. [CrossRef]

2. Balapure, K.; Bhatt, N.; Madamwar, D. Mineralization of reactive azo dyes present in simulated textile waste water using down flow microaerophilic fixed film bioreactor. *Bioresour. Technol.* **2015**, *175*, 1–7. [CrossRef] [PubMed]

3. Ahmadi, S.; Rahdar, A.; Igwegbe, C.A.; Mortazavi-Derazkola, S.; Banach, A.M.; Rahdar, S.; Singh, A.K.; Rodriguez-Couto, S.; Kyzas, G.Z. Praseodymium-doped cadmium tungstate (CdWO$_4$) nanoparticles for dye degradation with sonocatalytic process. *Polyhedron* **2020**, *190*, 114792. [CrossRef]

4. Cubas, P.d.J.; Semkiw, A.W.; Monteiro, F.C.; Weinert, P.L.; Monteiro, J.F.H.L.; Fujiwara, S.T. Synthesis of CuCr$_2$O$_4$ by self-combustion method and photocatalytic activity in the degradation of Azo Dye with visible light. *J. Photochem. Photobiol. A Chem.* **2020**, *401*, 112797. [CrossRef]

5. Gholami, P.; Khataee, A.; Soltani, R.D.C.; Bhatnagar, A. A review on carbon-based materials for heterogeneous sonocatalysis: Fundamentals, properties and applications. *Ultrason. Sonochem.* **2019**, *58*, 104681. [CrossRef]

6. Karaca, S.; Onal, E.Ç.; Açışlı, O.; Khataee, A. Preparation of chitosan modified montmorillonite biocomposite for sonocatalysis of dyes: Parameters and degradation mechanism. *Mater. Chem. Phys.* **2021**, *260*, 124125. [CrossRef]

7. Liu, M.; Yin, W.; Qian, F.J.; Zhao, T.L.; Yao, Q.Z.; Fu, S.Q.; Zhou, G.T. A novel synthesis of porous TiO$_2$ nanotubes and sequential application to dye contaminant removal and Cr(VI) visible light catalytic reduction. *J. Environ. Chem. Eng.* **2020**, *8*, 104061. [CrossRef]

8. Shan, R.; Lu, L.; Gu, J.; Zhang, Y.; Yuan, H.; Chen, Y.; Luo, B. Photocatalytic degradation of methyl orange by Ag/TiO$_2$/biochar composite catalysts in aqueous solutions. *Mater. Sci. Semicond. Process.* **2020**, *114*, 105088. [CrossRef]

9. Kumaravel, V.; Mathew, S.; Bartlett, J.; Pillai, S.C. Photocatalytic hydrogen production using metal doped TiO$_2$: A review of recent advances. *Appl. Catal. B Environ.* **2019**, *244*, 1021–1064. [CrossRef]

10. Fiorenza, R.; Di Mauro, A.; Cantarella, M.; Gulino, A.; Spitaleri, L.; Privitera, V.; Impellizzeri, G. Molecularly imprinted N-doped TiO$_2$ photocatalysts for the selective degradation of o-phenylphenol fungicide from water. *Mater. Sci. Semicond. Process.* **2020**, *112*, 105019. [CrossRef]

11. Zimbone, M.; Cacciato, G.; Spitaleri, L.; Egdell, R.G.; Grimaldi, M.G.; Gulino, A. Sb-doped titanium oxide: A rationale for its photocatalytic activity for environmental remediation. *ACS Omega* **2018**, *3*, 11270–11277. [CrossRef] [PubMed]

12. Peña-Velasco, G.; Hinojosa-Reyes, L.; Morán-Quintanilla, G.A.; Hernández-Ramírez, A.; Villanueva-Rodríguez, M.; Guzmán-Mar, J.L. Synthesis of heterostructured catalyst coupling MOF derived Fe$_2$O$_3$ with TiO$_2$ for enhanced photocatalytic activity in anti-inflammatory drugs mixture degradation. *Ceram. Int.* **2021**, *47*, 24632–24640. [CrossRef]

13. Baran, T.; Wojtyła, S.; Minguzzi, A.; Rondinini, S.; Vertova, A. Achieving efficient H$_2$O$_2$ production by a visible-light absorbing, highly stable photosensitized TiO$_2$. *Appl. Catal. B Environ.* **2019**, *244*, 303–312. [CrossRef]

14. Hamed, N.K.A.; Ahmad, M.K.; Hairom, N.H.H.; Faridah, A.B.; Mamat, M.H.; Mohamed, A.; Suriani, A.B.; Nafarizal, N.; Fazli, F.I.M.; Mokhtar, S.M.; et al. Dependence of photocatalysis on electron trapping in Ag-doped flowerlike rutile-phase TiO$_2$ film by facile hydrothermal method. *Appl. Surf. Sci.* **2020**, *534*, 147571. [CrossRef]

15. May-Lozano, M.; Lopez-Medina, R.; Mendoza Escamilla, V.; Rivadeneyra-Romero, G.; Alonzo-Garcia, A.; Morales-Mora, M.; González-Díaz, M.O.; Martinez-Degadillo, S.A. Intensification of the Orange II and Black 5 degradation by sonophotocatalysis using Ag-graphene oxide/TiO$_2$ systems. *Chem. Eng. Process. Process. Intensif.* **2020**, *158*, 108175. [CrossRef]

16. Mishra, S.; Cheng, L.; Maiti, A. The utilization of agro-biomass/byproducts for effective bio-removal of dyes from dyeing wastewater: A comprehensive review. *J. Environ. Chem. Eng.* **2021**, *9*, 104901. [CrossRef]

17. Misra, N.; Rawat, S.; Goel, N.K.; Shelkar, S.A.; Kumar, V. Radiation grafted cellulose fabric as reusable anionic adsorbent: A novel strategy for potential large-scale dye wastewater remediation. *Carbohydr. Polym.* **2020**, *249*, 116902. [CrossRef] [PubMed]

18. Oyewo, O.A.; Elemike, E.E.; Onwudiwe, D.C.; Onyango, M.S. Metal oxide-cellulose nanocomposites for the removal of toxic metals and dyes from wastewater. *Int. J. Biol. Macromol.* **2020**, *164*, 2477–2496. [CrossRef] [PubMed]

19. Koesoemadinata, V.C.; Chou, K.; Baharin, N.S.K.; Yahya, W.J.; Yuzir, M.A.M.; Akhir, F.N.M.; Iwamoto, K.; Hata, S.; Aid, S.R.B.; Othman, N.; et al. The effectiveness of biological pretreatment of oil palm empty fruit bunch on its conversion into Bio-Coke. *Bioresour. Technol. Reports* **2021**, *15*, 100765. [CrossRef]

20. Lefatshe, K.; Muiva, C.M.; Kebaabetswe, L.P. Extraction of nanocellulose and in-situ casting of ZnO/cellulose nanocomposite with enhanced photocatalytic and antibacterial activity. *Carbohydr. Polym.* **2017**, *164*, 301–308. [CrossRef]

21. Zhang, Z.; Wang, C.C.; Zakaria, R.; Ying, J.Y. Role of particle size in nanocrystalline TiO_2-based photocatalysts. *J. Phys. Chem. B* **1998**, *102*, 10871–10878. [CrossRef]

22. Lu, W.; Gao, S.; Wang, J. One-pot synthesis of Ag/ZnO self-assembled 3D hollow microspheres with enhanced photocatalytic performance. *J. Phys. Chem. C* **2008**, *112*, 16792–16800. [CrossRef]

23. Cai, Y.; Tan, F.; Qiao, X.; Wang, W.; Chen, J.; Qiu, X. Room-temperature synthesis of silica supported silver nanoparticles in basic ethanol solution and their antibacterial activity. *RSC Adv.* **2016**, *6*, 18407–18412. [CrossRef]

24. Ng, H.K.M.; Leo, C.P. Translucent and adsorptive PVA thin film containing microfibrillated cellulose intercalated with TiO_2 nanoparticles for dye removal. *Colloids Surf. A Physicochem. Eng. Asp.* **2019**, *578*, 123590. [CrossRef]

25. Zhang, Z.; Zhu, M.; Zhang, D. A thermogravimetric study of the characteristics of pyrolysis of cellulose isolated from selected biomass. *Appl. Energy* **2018**, *220*, 87–93. [CrossRef]

26. Dong, P.; Cheng, X.; Jin, Z.; Huang, Z.; Nie, X.; Wang, X.; Zhang, X. The green synthesis of Ag-loaded photocatalyst via DBD cold plasma assisted deposition of Ag nanoparticles on N-doped TiO_2 nanotubes. *J. Photochem. Photobiol. A Chem.* **2019**, *382*, 111971. [CrossRef]

27. Barakat, N.A.M.; Erfan, N.A.; Mohammed, A.A.; Mohamed, S.E.I. Ag-decorated TiO_2 nanofibers as Arrhenius equation-incompatible and effective photocatalyst for water splitting under visible light irradiation. *Colloids Surf. A Physicochem. Eng. Asp.* **2020**, *604*, 125307. [CrossRef]

28. Deng, S.; Zhang, Y.; Xie, D.; Yang, L.; Wang, G.; Zheng, X.S.; Zhu, J.; Wang, X.; Yu, Y.; Pan, G.; et al. Oxygen vacancy modulated $Ti_2Nb_{10}O_{29-x}$ embedded onto porous bacterial cellulose carbon for highly efficient lithium ion storage. *Nano Energy* **2019**, *58*, 355–364. [CrossRef]

29. Gogoi, D.; Namdeo, A.; Golder, A.K.; Peela, N.R. Ag-doped TiO_2 photocatalysts with effective charge transfer for highly efficient hydrogen production through water splitting. *Int. J. Hydrog. Energy* **2020**, *45*, 2729–2744. [CrossRef]

30. Singh, M.; Pahal, V.; Ahuja, D. Isolation and characterization of microfibrillated cellulose and nanofibrillated cellulose with "biomechanical hotspots". *Carbohydr. Polym.* **2020**, *234*, 115827. [CrossRef]

31. Komaraiah, D.; Radha, E.; Sivakumar, J.; Ramana Reddy, M.V.; Sayanna, R. Photoluminescence and photocatalytic activity of spin coated Ag^+ doped anatase TiO_2 thin films. *Opt. Mater. (Amst).* **2020**, *108*, 110401. [CrossRef]

32. Pandey, P.H.; Pawar, H.S. Cu dispersed TiO_2 catalyst for direct hydrogenation of carbon dioxide into formic acid. *J. CO2 Util.* **2020**, *41*, 101267. [CrossRef]

33. Messaoud, M.; Trabelsi, F.; Kumari, P.; Merenda, A.; Dumée, L.F. Recrystallization and coalescence kinetics of TiO_2 and ZnO nano-catalysts towards enhanced photocatalytic activity and colloidal stability within slurry reactors. *Mater. Chem. Phys.* **2020**, *252*, 123235. [CrossRef]

34. Islam, M.A.; Ong, H.L.; Villagracia, A.R.; Halim, K.A.A.; Ganganboina, A.B.; Doong, R.A. Biomass–derived cellulose nanofibrils membrane from rice straw as sustainable separator for high performance supercapacitor. *Ind. Crops Prod.* **2021**, *170*, 113694. [CrossRef]

35. Jayapriya, M.; Arulmozhi, M. *Beta vulgaris* peel extract mediated synthesis of Ag/TiO_2 nanocomposite: Characterization, evaluation of antibacterial and catalytic degradation of textile dyes-an electron relay effect. *Inorg. Chem. Commun.* **2021**, *128*, 108529. [CrossRef]

36. Dey, D.; Halder, N.; Misra, K.P.; Chattopadhyay, S.; Jain, S.K.; Bera, P.; Kumar, N.; Mukhopadhyay, A.K. Systematic study on the effect of Ag doping in shaping the magnetic properties of sol-gel derived TiO_2 nanoparticles. *Ceram. Int.* **2020**, *46*, 27832–27848. [CrossRef]

37. Al-Mamun, M.R.; Karim, M.N.; Nitun, N.A.; Kader, S.; Islam, M.S.; Khan, M.Z.H. Photocatalytic performance assessment of GO and Ag co-synthesized TiO_2 nanocomposite for the removal of methyl orange dye under solar irradiation. *Environ. Technol. Innov.* **2021**, *22*, 101537. [CrossRef]

38. Reddy, K.O.; Maheswari, C.U.; Dhlamini, M.S.; Mothudi, B.M.; Zhang, J.; Zhang, J.; Nagarajan, R.; Rajulu, A.V. Preparation and characterization of regenerated cellulose films using borassus fruit fibers and an ionic liquid. *Carbohydr. Polym.* **2017**, *160*, 203–211. [CrossRef]

39. Ng, H.K.M.; Leo, C.P. The coherence between TiO_2 nanoparticles and microfibrillated cellulose in thin film for enhanced dispersal and photodegradation of dye. *Prog. Org. Coatings* **2019**, *132*, 70–75. [CrossRef]

40. Zhou, P.; Shen, Y.; Zhao, S.; Bai, J.; Han, C.; Liu, W.; Wei, D. Facile synthesis of clinoptilolite-supported Ag/TiO_2 nanocomposites for visible-light degradation of xanthates. *J. Taiwan Inst. Chem. Eng.* **2021**, *122*, 231–240. [CrossRef]

41. Lopes, F.C.S.M.R.; da Rocha, M.D.G.C.; Bargiela, P.; Sousa Ferreira, H.; Pires, C.A.D.M. Ag/TiO_2 photocatalyst immobilized onto modified natural fibers for photodegradation of anthracene. *Chem. Eng. Sci.* **2020**, *227*, 115939. [CrossRef]

42. Kruk, M.; Jaroniec, M. Gas adsorption characterization of ordered organic-inorganic nanocomposite materials. *Chem. Mater.* **2001**, *13*, 3169–3183. [CrossRef]

43. Zhang, L.; Wan, J.; Hu, Z.; Jiang, W. Preparation and photocatalytic activity of TiO$_2$-wrapped cotton nanofiber composite catalysts. *BioResources* **2017**, *12*, 6062–6081. [CrossRef]

44. Alothman, Z.A. A review: Fundamental aspects of silicate mesoporous materials. *Materials* **2012**, *5*, 2874–2902. [CrossRef]

45. Lawal, A.A.; Hassan, M.A.; Zakaria, M.R.; Yusoff, M.Z.M.; Norrrahim, M.N.F.; Mokhtar, M.N.; Shirai, Y. Effect of oil palm biomass cellulosic content on nanopore structure and adsorption capacity of biochar. *Bioresour. Technol.* **2021**, *332*, 125070. [CrossRef] [PubMed]

46. Zhu, Y.; Wang, X.; Li, Z.; Fan, Y.; Zhang, X.; Chen, J.; Zhang, Y.; Dong, C.; Zhu, Y. Husbandry waste derived coralline-like composite biomass material for efficient heavy metal ions removal. *Bioresour. Technol.* **2021**, *337*, 125408. [CrossRef] [PubMed]

47. Li, Y.; Zhang, J.; Zhan, C.; Kong, F.; Li, W.; Yang, C.; Hsiao, B.S. Facile synthesis of TiO$_2$/CNC nanocomposites for enhanced Cr(VI) photoreduction: Synergistic roles of cellulose nanocrystals. *Carbohydr. Polym.* **2020**, *233*, 115838. [CrossRef] [PubMed]

48. Lu, L.; Wang, G.; Xiong, Z.; Hu, Z.; Liao, Y.; Wang, J.; Li, J. Enhanced photocatalytic activity under visible light by the synergistic effects of plasmonics and Ti^{3+}-doping at the Ag/TiO$_{2-x}$ heterojunction. *Ceram. Int.* **2020**, *46*, 10667–10677. [CrossRef]

49. Li, G.; Sun, Y.; Zhang, Q.; Gao, Z.; Sun, W.; Zhou, X. Ag quantum dots modified hierarchically porous and defective TiO$_2$ nanoparticles for improved photocatalytic CO$_2$ reduction. *Chem. Eng. J.* **2021**, *410*, 128397. [CrossRef]

50. de M. Oliveira, A.C.; dos Santos, M.S.; Brandão, L.M.S.; de Resende, I.T.F.; Leo, I.M.; Morillo, E.S.; Yerga, R.M.N.; Fierro, J.L.G.; da S. Egues, S.M.; Figueiredo, R.T. The effect of cellulose loading on the photoactivity of cellulose-TiO$_2$ hybrids for hydrogen production under simulated sunlight. *Int. J. Hydrog. Energy* **2017**, *42*, 28747–28754. [CrossRef]

51. Yang, J.; Luo, X. Ag-doped TiO$_2$ immobilized cellulose-derived carbon beads: One-Pot preparation, photocatalytic degradation performance and mechanism of ceftriaxone sodium. *Appl. Surf. Sci.* **2021**, *542*, 148724. [CrossRef]

52. Yu, Y.; Zhu, X.; Wang, L.; Wu, F.; Liu, S.; Chang, C.; Luo, X. A simple strategy to design 3-layered Au-TiO$_2$ dual nanoparticles immobilized cellulose membranes with enhanced photocatalytic activity. *Carbohydr. Polym.* **2020**, *231*, 115694. [CrossRef] [PubMed]

53. Xue, X.; Gong, X.; Chen, X.; Chen, B.Y. A facile synthesis of Ag/Ag$_2$O@TiO$_2$ for toluene degradation under UV–visible light: Effect of Ag formation by partial reduction of Ag$_2$O on photocatalyst stability. *J. Phys. Chem. Solids* **2021**, *150*, 109799. [CrossRef]

54. Wang, B.B.; Zhong, X.X.; Zhu, J.; Wang, Y.; Zhang, Y.; Cvelbar, U.; Ostrikov, K. Single-step synthesis of TiO$_2$/WO$_{3-x}$ hybrid nanomaterials in ethanoic acid: Structure and photoluminescence properties. *Appl. Surf. Sci.* **2021**, *562*, 150180. [CrossRef]

55. Lin, Z.; Huang, J. A hierarchical H$_3$PW$_{12}$O$_{40}$/TiO$_2$ nanocomposite with cellulose as scaffold for photocatalytic degradation of organic pollutants. *Sep. Purif. Technol.* **2021**, *264*, 118427. [CrossRef]

56. Liu, M.; Kuang, K.; Li, G.; Yang, S.; Yuan, Z. Photoluminescence-enhanced cholesteric films: Coassembling copper nanoclusters with cellulose nanocrystals. *Carbohydr. Polym.* **2021**, *257*, 117641. [CrossRef]

57. Shanthini, G.M.; Sakthivel, N.; Menon, R.; Nabhiraj, P.Y.; Gómez-Tejedor, J.A.; Meseguer-Dueñas, J.M.; Gómez Ribelles, J.L.; Krishna, J.B.M.; Kalkura, S.N. Surface stiffening and enhanced photoluminescence of ion implanted cellulose–polyvinyl alcohol–silica composite. *Carbohydr. Polym.* **2016**, *153*, 619–630. [CrossRef]

58. Mahnae, S.; Hadavi, M.S.; Azizi, H.R. Effect of silver coating on the optical, morphological, PL and crystal structure of Ag–TiO$_2$ thin films. *Opt. Mater. (Amst).* **2021**, *115*, 111056. [CrossRef]

59. Sboui, M.; Lachheb, H.; Bouattour, S.; Gruttadauria, M.; La Parola, V.; Liotta, L.F.; Boufi, S. TiO$_2$/Ag$_2$O immobilized on cellulose paper: A new floating system for enhanced photocatalytic and antibacterial activities. *Environ. Res.* **2021**, *198*, 111257. [CrossRef]

60. Albu, S.P.; Ghicov, A.; Aldabergenova, S.; Drechsel, P.; LeClere, D.; Thompson, G.E.; Macak, J.M.; Schmuki, P. Formation of double-walled TiO$_2$ nanotubes and robust anatase membranes. *Adv. Mater.* **2008**, *20*, 4135–4139. [CrossRef]

61. Fiorenza, R.; Di Mauro, A.; Cantarella, M.; Iaria, C.; Scalisi, E.M.; Brundo, M.V.; Gulino, A.; Spitaleri, L.; Nicotra, G.; Dattilo, S.; et al. Preferential removal of pesticides from water by molecular imprinting on TiO$_2$ photocatalysts. *Chem. Eng. J.* **2020**, *379*, 122309. [CrossRef]

62. Shi, Y.; Yang, D.; Li, Y.; Qu, J.; Yu, Z.Z. Fabrication of PAN@TiO$_2$/Ag nanofibrous membrane with high visible light response and satisfactory recyclability for dye photocatalytic degradation. *Appl. Surf. Sci.* **2017**, *426*, 622–629. [CrossRef]

63. Zheng, A.L.T.; Sabidi, S.; Ohno, T.; Maeda, T.; Andou, Y. Cu$_2$O/TiO$_2$ decorated on cellulose nanofiber/reduced graphene hydrogel for enhanced photocatalytic activity and its antibacterial applications. *Chemosphere* **2022**, *286*, 131731. [CrossRef]

64. Zhu, X.; Shen, S.; Tang, Z.; Yang, J. Ti^{3+}-doped TiO$_2$@C nanorods with enhanced photocatalytic performance under visible light. *Compos. Interfaces* **2020**, *27*, 263–275. [CrossRef]

65. Fu, G.; Zhou, P.; Zhao, M.; Zhu, W.; Yan, S.; Yu, T.; Zou, Z. Carbon coating stabilized Ti^{3+}-doped TiO$_2$ for photocatalytic hydrogen generation under visible light irradiation. *Dalt. Trans.* **2015**, *44*, 12812–12817. [CrossRef] [PubMed]

66. Wang, Y.; Zhang, M.; Lv, S.; Li, X.; Wang, D.; Song, C. Photogenerated oxygen vacancies in hierarchical Ag/TiO$_2$ nanoflowers for enhanced photocatalytic reactions. *ACS Omega* **2020**, *5*, 13994–14005. [CrossRef] [PubMed]

67. Zhang, Y.; Li, Y.; Yu, H.; Yu, K.; Yu, H. Interfacial defective Ti^{3+} on Ti/TiO$_2$ as visible-light responsive sites with promoted charge transfer and photocatalytic performance. *J. Mater. Sci. Technol.* **2021**. [CrossRef]

68. Saroj, S.; Singh, L.; Singh, S.V. Solution-combustion synthesis of anion (iodine) doped TiO$_2$ nanoparticles for photocatalytic degradation of Direct Blue 199 dye and regeneration of used photocatalyst. *J. Photochem. Photobiol. A Chem.* **2020**, *396*, 112532. [CrossRef]

69. Lin, J.J.; Raj, R.K.; Wang, S.; Kokkonen, E.; Mikkelä, M.H.; Urpelainen, S.; Prisle, N.L. Pre-deliquescent water uptake in deposited nanoparticles observed with in situ ambient pressure X-ray photoelectron spectroscopy. *Atmos. Chem. Phys.* **2021**, *21*, 4709–4727. [CrossRef]

70. Friedman, A.K.; Shi, W.; Losovyj, Y.; Siedle, A.R.; Baker, L.A. Mapping microscale chemical heterogeneity in Nafion membranes with X-ray photoelectron spectroscopy. *J. Electrochem. Soc.* **2018**, *165*, H733–H741. [CrossRef]

71. Mohamed, M.A.; Salleh, W.N.W.; Jaafar, J.; Ismail, A.F.; Abd Mutalib, M.; Jamil, S.M. Incorporation of N-doped TiO_2 nanorods in regenerated cellulose thin films fabricated from recycled newspaper as a green portable photocatalyst. *Carbohydr. Polym.* **2015**, *133*, 429–437. [CrossRef]

72. Das, D.; Hussain, S.; Ghosh, A.K.; Pal, A.K. Studies on cellulose nanocrystals extracted from *Musa sapientum*: Structural and bonding aspects. *Cellul. Chem. Technol.* **2018**, *52*, 729–739.

73. Ma, X.; Chen, Y. Preparation and characterization of Mn/N co-doped TiO_2 loaded on wood-based activated carbon fiber and its visible light Photodegradation. *Polymers* **2015**, *7*, 1660–1673. [CrossRef]

74. Motora, K.G.; Wu, C.; Xu, T.; Chala, T.F.; Lai, C. Photocatalytic, antibacterial, and deodorization activity of recycled triacetate cellulose nanocomposites. *Mater. Chem. Phys.* **2020**, *240*, 122260. [CrossRef]

75. Xiao, G.; Zhang, X.; Zhang, W.; Zhang, S.; Su, H.; Tan, T. Visible-light-mediated synergistic photocatalytic antimicrobial effects and mechanism of Ag-nanoparticles@chitosan-TiO_2 organic-inorganic composites for water disinfection. *Appl. Catal. B Environ.* **2015**, *170–171*, 255–262. [CrossRef]

76. Voisin, H.; Falourda, X.; Rivard, C.; Capron, I. Versatile nanocellulose-anatase TiO_2 hybrid nanoparticles in Pickering emulsions for the photocatalytic degradation of organic and aqueous dyes. *JCIS Open* **2021**, *3*, 100014. [CrossRef]

77. Nsib, M.F.; Hajji, F.; Mayoufi, A.; Moussa, N.; Rayes, A.; Houas, A. In situ synthesis and characterization of TiO_2/HPM cellulose hybrid material for the photocatalytic degradation of 4-NP under visible light. *Comptes Rendus Chim.* **2014**, *17*, 839–848. [CrossRef]

78. Al-Mamun, M.R.; Kader, S.; Islam, M.S.; Khan, M.Z.H. Photocatalytic activity improvement and application of UV-TiO_2 photocatalysis in textile wastewater treatment: A review. *J. Environ. Chem. Eng.* **2019**, *7*, 103248. [CrossRef]

79. Lan, L.; Shao, Y.; Jiao, Y.; Zhang, R.; Hardacre, C.; Fan, X. Systematic study of H_2 production from catalytic photoreforming of cellulose over Pt catalysts supported on TiO_2. *Chinese J. Chem. Eng.* **2020**, *28*, 2084–2091. [CrossRef]

80. Guillard, C.; Lachheb, H.; Houas, A.; Ksibi, M.; Elaloui, E.; Herrmann, J.M. Influence of chemical structure of dyes, of pH and of inorganic salts on their photocatalytic degradation by TiO_2 comparison of the efficiency of powder and supported TiO_2. *J. Photochem. Photobiol. A Chem.* **2003**, *158*, 27–36. [CrossRef]

81. Zhang, H.; Wei, C.; Huang, Y.; Wang, J. Preparation of cube micrometer potassium niobate ($KNbO_3$) by hydrothermal method and sonocatalytic degradation of organic dye. *Ultrason. Sonochem.* **2016**, *30*, 61–69. [CrossRef] [PubMed]

82. Wang, J.; Guo, Y.; Liu, B.; Jin, X.; Liu, L.; Xu, R.; Kong, Y.; Wang, B. Detection and analysis of reactive oxygen species (ROS) generated by nano-sized TiO_2 powder under ultrasonic irradiation and application in sonocatalytic degradation of organic dyes. *Ultrason. Sonochem.* **2011**, *18*, 177–183. [CrossRef] [PubMed]

83. Wang, J.; Jiang, Y.; Zhang, Z.; Zhao, G.; Zhang, G.; Ma, T.; Sun, W. Investigation on the sonocatalytic degradation of congo red catalyzed by nanometer rutile TiO_2 powder and various influencing factors. *Desalination* **2007**, *216*, 196–208. [CrossRef]

84. Li, S.; Zhang, M.; Ma, X.; Qiao, J.; Zhang, H.; Wang, J.; Song, Y. Preparation of ortho-symmetric double (OSD) Z-scheme SnO_2\CdSe/Bi_2O_3 sonocatalyst by ultrasonic-assisted isoelectric point method for effective degradation of organic pollutants. *J. Ind. Eng. Chem.* **2019**, *72*, 157–169. [CrossRef]

85. Wang, J.; Wang, Z.; Vieira, C.L.Z.; Wolfson, J.M.; Pingtian, G.; Huang, S. Review on the treatment of organic pollutants in water by ultrasonic technology. *Ultrason. Sonochem.* **2019**, *55*, 273–278. [CrossRef]

86. Lops, C.; Ancona, A.; Di Cesare, K.; Dumontel, B.; Garino, N.; Canavese, G.; Hérnandez, S.; Cauda, V. Sonophotocatalytic degradation mechanisms of Rhodamine B dye via radicals generation by micro- and nano-particles of ZnO. *Appl. Catal. B Environ.* **2019**, *243*, 629–640. [CrossRef]

87. Samanta, M.; Mukherjee, M.; Ghorai, U.K.; Bose, C.; Chattopadhyay, K.K. Room temperature processed copper phthalocyanine nanorods: A potential sonophotocatalyst for textile dye removal. *Mater. Res. Bull.* **2020**, *123*, 110725. [CrossRef]

88. Urushidate, K.; Hara, K.; Yoshiba, M.; Kojima, T.; Itoi, T.; Izumi, Y. Optimization of high voltage-type solar cell comprising thin TiO_2 on anode and thin Ag–TiO_2 photocatalysts on cathode. *Sol. Energy* **2020**, *208*, 604–611. [CrossRef]